

A Detailed Observational Study of Molecular Loops 1 and 2 in the Galactic Center

Kazufumi TORII,¹ Natsuko KUDO,¹ Motosuji FUJISHITA,¹ Tokuchi KAWASE,¹
 Hiroaki YAMAMOTO,¹ Akiko KAWAMURA,¹ Norikazu MIZUNO,² Toshikazu ONISHI,³
 Akira MIZUNO,⁴ Mami MACHIDA,⁵ Kunio TAKAHASHI,⁶ Satoshi NOZAWA,⁷
 Ryoji MATSUMOTO,⁸ and Yasuo FUKUI¹

¹*Department of Astrophysics, Nagoya University, Chikusa-ku, Nagoya 464-8602, Japan*

²*National Astronomical Observatory of Japan, Osawa, Mitaka, Tokyo 181-8588, Japan*

³*Department of Physical Science, Osaka prefecture University, Sakai, Osaka 599-8531, Japan*

⁴*Solar-Terrestrial Environment Laboratory, Nagoya University, Chikusa-ku, Nagoya 464-8601, Japan*

⁵*Department of Physics, Kyushu University, 6-10-1 Hakozaki, Higashi-ku, Fukuoka, Fukuoka 812-8581, Japan*

⁶*Japan Agency for Marine-Earth Science and Technology, Kanazawa-ku, Yokohama, Kanagawa 236-0001, Japan*

⁷*Department of Science, Ibaraki University, 2-1-1 Bunkyo, Mito, Ibaraki 310-8512, Japan*

⁸*Faculty of Science, Chiba University, Inage-ku, Chiba 263-8522, Japan*
torii@a.phys.nagoya-u.ac.jp, fukui@a.phys.nagoya-u.ac.jp

(Received 2009 April 3; accepted 0 0)

Abstract

Fukui et al. (2006) discovered two huge molecular loops in the Galactic center located in $(l, b) \simeq (355^\circ\text{--}359^\circ, 0^\circ\text{--}2^\circ)$ in a large velocity range of $-180\text{--}40$ km s⁻¹. Following the discovery, we present detailed observational properties of the two loops based on NANTEN ¹²CO($J=1-0$) and ¹³CO($J=1-0$) datasets at 10 pc resolution including a complete set of velocity channel distributions and comparisons with HI and dust emissions as well as with the other broad molecular features. We find new features on smaller scales in the loops including helical distributions in the loop tops and vertical spurs. The loops have counterparts of the HI gas indicating that the loops include atomic gas. The IRAS far infrared emission is also associated with the loops and was used to derive an X-factor of $0.7(\pm 0.1) \times 10^{20}$ cm⁻² (K km s⁻¹)⁻¹ to convert the ¹²CO intensity into the total molecular hydrogen column density. From the ¹²CO, ¹³CO, HI and dust datasets we estimated the total mass of loops 1 and 2 to be $\sim 1.4 \times 10^6 M_\odot$ and $\sim 1.9 \times 10^6 M_\odot$, respectively, where the HI mass corresponds to $\sim 10\text{--}20$ % of the total mass and the total kinetic energy of the two loops to be $\sim 10^{52}$ ergs. An analysis of the kinematics of the loops yields that the loops are

rotating at $\sim 47 \text{ km s}^{-1}$ and expanding at $\sim 141 \text{ km s}^{-1}$ at a radius of 670 pc from the center. Fukui et al. (2006) presented a model that the loops are created by the magnetic flotation due to the Parker instability with an estimated magnetic field strength of $\sim 150 \mu\text{G}$. We present comparisons with the recent numerical simulations of the magnetized nuclear disk by Machida et al. (2009) and Takahashi et al. (2009) and show that the theoretical results are in good agreements with the observations. The helical distributions also suggest that some magnetic instability plays a role similarly to the solar helical features.

Key words: Radio lines: ISM—ISM: clouds—ISM: magnetic fields—magnetic loops

1. Introduction

The evolution of molecular gas may be significantly different in the central region of a grand-design galaxy from that in the disk because the strong gravitational field by high stellar density makes the pressure much higher in the central region than in the disk. It is important to understand the distributions and physical conditions of molecular gas in the Galactic center and their astronomical implications in our continuing efforts to elucidate galactic evolution.

Previous studies of the Galactic center show that most of the molecular gas is concentrated in the inner 300 pc which is called the "Central Molecular Zone" (hereafter CMZ, e.g., Morris & Serabyn 1996). The CMZ including Sgr A and Sgr B2 molecular clouds has been a region intensively studied (e.g., Fukui et al. 1977; Scoville, Solomon & Penzias 1975; Güsten & Henkel 1983). The molecular gas in the CMZ is characterized by high temperatures, $\sim 30\text{--}300$ K, as derived by observations in CO, NH₃, H₂, H₃⁺ lines (Martin et al. 2004; Hüttemeister et al. 1993; Rodríguez-Fernández et al. 2001; Oka et al. 2005; Nagai et al. 2007), and by violent motions of $1\sigma \simeq 15\text{--}50 \text{ km s}^{-1}$ (e.g., Morris & Serabyn 1996; Güsten & Philipp 2004). The origin of these two characteristics has not been understood well in the last few decades, whereas a few mechanisms to drive gas motion including the stellar bar potential and supernova explosions have been discussed (e.g., Binney et al. 1991; Liszt 2006; Oka et al. 2007). The Galactic center is also characterized by strong magnetic field. Radio Arc and the non-thermal filaments (Yusef-Zadeh, Morris & Chance 1984; Yusef-Zadeh, Hewitt & Cotton 2004) and, perhaps the infrared double helix (Morris, Uchida & Do 2006), strongly suggest existence of quite unique magnetic field structures in the Galactic center with the field strength as large as 1 mG. Most recently, Crocker et al. (2010) summarized previous observations of radio synchrotron emission in a frequency range of 1.4–10 GHz and derived the Galactic center field to be at least $\sim 50 \mu\text{G}$ on 400 pc scales. There are also unusually broad molecular features with weaker intensities outside the CMZ up to nearly 1 kpc from the center, e.g., Clump 1 ($l, b \simeq 355^\circ, 0^\circ$), Clump 2 ($l, b \simeq 3^\circ, 0^\circ$) and $l = 5.5^\circ$ complex ($l, b \simeq 5^\circ, 0^\circ$) (Bania 1977; Stark & Bania 1986; Liszt 2006),

whereas these features did not received much attention so far.

Fukui et al. (2006; hereafter Paper I) discovered two molecular loops toward $(l, b) \simeq (355^\circ\text{--}359^\circ, 0^\circ\text{--}2^\circ)$ by analyzing the $^{12}\text{CO}(J=1\text{--}0)$ NANTEN Galactic plane survey dataset and named them loops 1 and 2. These loops are distributed in a negative V_{LSR} of $-180\text{--}40$ km s^{-1} and have heights of ~ 2 degrees from the galactic plane which correspond to ~ 300 pc at the distance to the Galactic center, 8.5 kpc. The loops are characterized by the two bright foot points in CO emission on each end, and the foot points show large velocity dispersions of $\sim 50\text{--}100$ km s^{-1} . In addition, Science Online Material (SOM) of Paper I showed that Clump 2 and the $l = 5.5^\circ$ complex are connected by an off-plane loop-like feature and the authors suggested their similarity with loops 1 and 2. Subsequently, Fujishita et al. (2009; hereafter Paper II) discovered loop 3 which is located in the same direction with loops 1 and 2 in a positive velocity range of $V_{\text{LSR}} \simeq 20\text{--}200$ km s^{-1} . Loop 3 shows a loop-like outer shape and similar height and length with loops 1 and 2 and has two foot points with broad velocity dispersions on their ends.

These three loops are interpreted by magnetic flotation caused by the Parker instability (Parker 1966) in Papers I and II, where loops 1 and 2 offer the first observational evidence for the Parker’s model of cloud formation on the galactic scale. The Parker instability was numerically studied by Matsumoto et al. (1988) and its was shown that the foot point is a natural outcome of the falling motion of gas along the floated field lines and that the foot point often causes shocks. Most recently, Torii et al. (2010) presented a detailed analysis of the foot points between loops 1 and 2 by using multi- J CO transitions at 1–4 pc resolutions and derived kinetic temperature as high as $\sim 30\text{--}100\text{K}$ or more. The high temperature was interpreted as due to the shock heating in the foot point by the authors. In addition, they revealed that the foot point exhibits a characteristic U-shape and interpreted the shape in terms of the magnetic flotation picture.

Paper I, a Letter, described limited observational properties of loops 1 and 2. After the subsequent works reviewed above, it remains important to present observational details of loops 1 and 2 in order to pursue further the physical properties of the loops. We here present a full account of loops 1 and 2 from the ^{12}CO and ^{13}CO datasets of the NANTEN Galactic plane survey, along with comparisons with HI, dust and the other outstanding molecular features. Section 2 describes the $^{12}\text{CO}(J=1\text{--}0)$ and $^{13}\text{CO}(J=1\text{--}0)$ datasets. Detailed observational properties of the two loops are presented in Section 3. Sections 4, 5 and 6 show comparisons, mass estimates and a kinematical and morphological model, respectively. Section 7 presents discussion and Section 8 summarizes the paper.

2. NANTEN Datasets

The $^{12}\text{CO}(J=1\text{--}0)$ dataset at 115 GHz and the $^{13}\text{CO}(J=1\text{--}0)$ dataset at 110 GHz obtained by using the NANTEN 4m mm telescope in Chile toward the Galactic center were used in this study. Basic parameters of the observations are summarized in Table 1.

2.1. ^{12}CO

Observations were carried out during the period from March 1999 to September 2001. The half-power beamwidth (HPBW) was $2'.6$ at 115 GHz. NANTEN was equipped with a 4 K cryogenically cooled Nb superconductor-insulator-superconductor (SIS) mixer receiver (Ogawa et al. 1990). The typical system temperature was ~ 280 K in the single-side band, including the atmosphere toward the zenith. The spectrometer was an acousto-optical spectrometer (AOS) with 2048 channels. The frequency band-width and resolution were 250 MHz and 250 kHz, which correspond to a velocity coverage of 650 km s^{-1} and a velocity resolution of 0.65 km s^{-1} , respectively, at 115 GHz. The absolute intensity calibration from observed antenna temperature was done by observing rho-Oph East (R.A.(b1950.0), Dec.(b1950.0)= $16^{\text{h}}29^{\text{m}}20^{\text{s}}.9$, $-24^{\circ}22'13''$) every 2 hours, the absolute temperature of which was assumed to be 15 K. The telescope pointing was maintained within $20''$ by observing of planets at radio wavelength in addition to optical observations of stars with a CCD camera equipped with the telescope. The observed region was 240 square degrees toward $(l, b) \simeq (350^{\circ}-10^{\circ}, -5^{\circ}-5^{\circ})$ by using the position switching mode with a $4'$ grid spacing, which corresponds to 10 pc at 8.5 kpc. In total, 54,000 positions were observed. Typical r.m.s. (root mean square) noise fluctuations of 0.36 K were achieved at a velocity resolution of 0.65 km s^{-1} .

2.2. ^{13}CO

The $^{13}\text{CO}(J=1-0)$ dataset toward the Galactic center region was taken with the same instrument as the $^{12}\text{CO}(J=1-0)$ observations in October 2003. The half-power beam width (HPBW) was $2'.7$ at 110 GHz. The same receiver and spectrometer with $^{12}\text{CO}(J=1-0)$ were used. Typical system temperature was ~ 100 K in the single-side band, and a velocity coverage and a velocity resolution were 620 km s^{-1} and 0.62 km s^{-1} , respectively, at 110 GHz. The absolute intensity calibration was carried out by observing rho-Oph East (R.A.(b1950.0), Dec.(b1950.0)= $16^{\text{h}}29^{\text{m}}20^{\text{s}}.9$, $-24^{\circ}22'13''$) every 2 hours. We assumed absolute radiation temperature of rho-Oph East was 10 K. The observed region was toward $(l, b) \simeq (354^{\circ}-8^{\circ}, -1^{\circ}-1^{\circ})$ with the position-switching mode at a grid spacing of $2'$. In total, 25,200 positions were observed. Typical r.m.s. noise fluctuations were 0.20 K at a velocity resolution of 0.62 km s^{-1} .

3. CO distributions of loops 1 and 2

Figure 1 shows the large-scale distribution of ^{12}CO intensity in an area of $(l, b) \simeq (350^{\circ}-10^{\circ}, -5^{\circ}-5^{\circ})$ in $V_{\text{LSR}} \simeq -300-300 \text{ km s}^{-1}$. Figure 1a shows the distribution of the total ^{12}CO integrated intensity. In Figure 1a, most of the emission along the galactic plane is the 3-kpc expanding arm and the CMZ is dominant in $l \simeq 355^{\circ}-359^{\circ}$. Locations of loops 1 and 2 and loop 3 toward $l \simeq 355^{\circ}-359^{\circ}$ are shown by two boxes with broken lines in Figure 1a and Figure 1b. In Figure 1b, the longitude-velocity diagram, the molecular gas in the Galactic center region is seen as broad features whose velocity extents are a few tens km s^{-1} or more. The narrow

features near 0 km s^{-1} are clouds outside the Galactic center and the 3-kpc arm is seen as a narrow feature at $\sim -50 \text{ km s}^{-1}$ toward $l \simeq 0^\circ$ with a velocity gradient of $\sim 8 \text{ km s}^{-1} \text{ deg}^{-1}$.

Figure 2 shows the integrated intensity distributions for the negative and positive velocity ranges. Figures 2a and 2b show the distributions in the negative velocity range in the l - b plane and b - v plane, respectively, and loops 1 and 2 are indicated in Figure 2a. Figures 2c and 2d show the distributions in the positive velocity range in the l - b plane and b - v plane, respectively, and loop 3 is indicated in Figure 2c.

Figure 3 shows close-up images of ^{12}CO and ^{13}CO for loops 1 and 2 for two velocity ranges, from -180 to -90 km s^{-1} and from -90 to -40 km s^{-1} , in an area of $l \simeq 355^\circ$ – 359° and $b \simeq 0^\circ$ – 2° shown by a rectangle in Figure 2a¹. Figures 3a–d are for loop 1; Figures 3a and 3b are the l - b diagrams of ^{12}CO and ^{13}CO and Figures 3c and 3d are the l - v diagrams of ^{12}CO and ^{13}CO . Figures 3e–h are for loop 2; Figures 3e and 3f are the l - b diagrams of ^{12}CO and ^{13}CO and Figures 3g and 3h are the l - v diagrams of ^{12}CO and ^{13}CO .

Figure 3a shows that loop 1 is a remarkable filamentary feature of $\sim 30 \text{ pc}$ width and $\sim 300 \text{ pc}$ projected length, being elevated from the plane by $\sim 200 \text{ pc}$. It shows a bright spot at $(l, b) \simeq (356^\circ, 1^\circ)$, which has strong intensity gradients toward the plane and also toward the east. We also recognize a less enhanced peak toward $(l, b) \simeq (357.4^\circ, 0.8^\circ)$. We shall call these two peaks "foot points" following Paper I. Figure 3c shows that these two foot points have enhanced velocity extents of $\sim 50 \text{ km s}^{-1}$ or more. The ^{13}CO emission is significant only toward the foot point at $(l, b) \simeq (356^\circ, 1^\circ)$, while the observations does not cover the region above $b = 1^\circ$.

Figure 3e shows that loop 2 is an outstanding feature with a width of $\sim 30 \text{ pc}$ and a length of $\sim 400 \text{ pc}$ and is elevated by $\sim 300 \text{ pc}$ from the plane. A feature at $b \simeq 1.4^\circ$ extending toward the center is part of loop 1. Loop 2 shows two bright spots with enhanced velocity extents of $\sim 60 \text{ km s}^{-1}$ toward $(l, b) \simeq (355.4^\circ, 0.8^\circ)$ and $(356.1^\circ, 0.8^\circ)$. The ^{13}CO emission is detected toward these two spots (Figure 3c,d) although the coverage is limited to b less than $\sim 1^\circ$. We shall call these two spots "foot points" of loop 2 (Paper I).

Figure 4 shows typical ^{12}CO and ^{13}CO line profiles toward loops 1 and 2. These show the line profiles are not Gaussian but have shapes of peaked triangles. We note that the profiles toward the foot points show asymmetry with a strong skew. The velocity span is as large as 40 km s^{-1} toward the loop top and becomes even larger as 100 km s^{-1} toward the foot points.

Figures 5 and 6 show distributions of the intensity-weighted averaged velocity and 1?? velocity dispersion in the loops, respectively, where the velocity range is from -190 km s^{-1} to -30 km s^{-1} averaged with a single Gaussian function of a $10'$ FWHM. The larger beam size was taken in order to suppress small scale irregularities. We confirm the velocity gradients in Paper I and roughly estimate the gradients to be $\sim 0.2 \text{ km s}^{-1} \text{ pc}^{-1}$ and $\sim 0.35 \text{ km s}^{-1} \text{ pc}^{-1}$ along loops 1 and 2, respectively. We also find that the velocity dispersion in the foot points is

¹ The fits file of $^{12}\text{CO}(J=1-0)$ in the loops 1 and 2 region can be taken from <http://www.a.phys.nagoya-u.ac.jp/~torii/loop/eg>

significantly larger than that in the rest of the loops.

In order to show more details of the velocity distributions we present a series of velocity channel distributions every 10 km s^{-1} as 12 panels in Figure 7. We identify the foot points of loops 1 and 2 toward $l \simeq 355^\circ, 357^\circ$ and 359° at $b \simeq 0.8^\circ$. We find two new features in these panels; i.e., a vertical feature toward $(l, b) \simeq (356^\circ, 1.4^\circ\text{--}1.6^\circ)$ in V_{LSR} from -120 to -90 km s^{-1} between loops 1 and 2 and a vertical protrusion toward $(l, b) \simeq (355.4^\circ, 1.8^\circ\text{--}2.0^\circ)$ above the western foot point of loop 2. One of these features, which we tentatively calls "spurs", between loops 1 and 2 seems to be separated from loop 2 in its vertical direction.

In addition, we note that three regions show peculiar distributions that are not part of simple loops as shown in Figures 8, 9 and 10. We call hereafter these features in Figures 8 and 9 helical distributions.

Figure 8 shows the details of the top of loop 1 every 4 km s^{-1} from -129 to -107 km s^{-1} . The panels from -121 to -113 km s^{-1} show S-shaped distributions in a range $l \simeq 357.0^\circ\text{--}357.4^\circ$ and those from -115 to -113 km s^{-1} also show a similar feature in $(l, b) \simeq (356.8^\circ\text{--}357.3^\circ, 0.9^\circ)$.

Figure 9 shows the top of loop 2 every 4 km s^{-1} from -86 to -66 km s^{-1} . A peculiar peaked shape is found from $(l, b) \simeq (355.4^\circ\text{--}355.8^\circ, 1.8^\circ\text{--}2.1^\circ)$.

Figure 10 shows the area in the south of the foot point of loop 2. The panels from -50 to -42 km s^{-1} show a vertical feature at $l \simeq 355.6^\circ$ and the panels from -44 to -36 km s^{-1} indicate a bridge-like feature that connects this vertical feature and the local intensity peak at $(l, b) \simeq (355.0^\circ\text{--}355.2^\circ, 1.1^\circ)$ in panel from -44 to -40 km s^{-1} . In addition, the panel from -34 to -30 km s^{-1} shows another vertical feature in $(l, b) \simeq (355.2^\circ, 1.4^\circ\text{--}1.8^\circ)$.

To summarize the section, we note that the results in Paper I are basically confirmed in velocity channel distributions and that new features including spurs above the foot points and helical distributions in the loop tops are found.

4. Comparisons with the other broad CO features, HI and dust

4.1. The other broad CO features

There are a few CO features which have similar characteristics with loops 1 and 2 in the inner 1 kpc of the Galactic center; a loop-like shape with two foot points of broad velocity widths in the both ends of the loop. Paper II reported discovery of another molecular loop, loop 3, as observed in the CO $J=1\text{--}0$ transition. Loop 3 is distributed in the same direction with loops 1 and 2 in a positive velocity range of $V_{\text{LSR}} \simeq 20\text{--}200 \text{ km s}^{-1}$ (Figure 2c). Loop 3 shows a dome-like feature with broad foot points in the both ends and its inside is filled with the CO emission. The size and velocity spans of loop 3 are fairly similar to those of loops 1 and 2, and Paper II showed the foot points of loop 3 seem yet undeveloped because the mass of the foot points is significantly smaller than in the loop top as compared with loops 1 and 2 (Table 2, see also Table 4 of Paper II). It was suggested in Paper II that loop 3 is in an earlier

evolutionary stage than loops 1 and 2, because most of the floated gas in loop 3 still remains above the foot points. Paper II also showed that loop 3 is associated with HI having similar distribution and kinematics.

There are two outstanding CO clumps known as Clump 2 and the $l = 5.5^\circ$ complex at $l \simeq 3.0^\circ$ and $l \simeq 5.5^\circ$ and these clumps have very broad velocity widths of $\sim 100\text{--}150 \text{ km s}^{-1}$ (Bania 1977; Stark & Bania 1986; Boyce & Cohen 1994; Bitran et al. 1997; Liszt 2006). The NANTEN CO survey revealed a bridge-like feature connecting these two clumps in $(l, b) \simeq (3.6^\circ\text{--}4.8^\circ, 0.6^\circ\text{--}1.6^\circ)$ and $V_{\text{LSR}} \simeq 30\text{--}100 \text{ km s}^{-1}$ (in SOM of Paper I) at 10 pc resolution. This bridge-like feature is seen in the ^{12}CO images at 20 pc resolution in Bitran et al. (1997) (e.g., their Figure 5) but these authors gave no discussion on the feature. The feature was also discussed by Liszt (2008) as an inward flow from the outside of the Galactic center, but did not discuss the loop interpretation by Fukui et al. (2006). Boyce & Cohen (1994) detected the bridge-like feature in OH absorption and name it Clump 4 and Filament B but did not discuss the nature of the feature. The other previous studies cover only lower latitudes below the connecting feature.

The two clumps show elongation vertical to the galactic plane with sizes around 75 pc times 135 pc (Clump 2) and around 50 pc times 100 pc (the $l = 5.5^\circ$ complex), respectively, and such vertical elongation is similar to the foot points of loops 1 and 2. Their sizes are a few times larger than those of the foot points of loops 1 and 2. As derived later in Section 5, the molecular masses of the foot points of loops 1 and 2 are in the order of $(1\text{--}6) \times 10^5 M_\odot$, several times smaller than those of Clump 2 and the $l = 5.5^\circ$ complex having $(2\text{--}6) \times 10^6 M_\odot$ (Table 2, Bania 1977; Stark & Bania 1986). The two clumps, therefore, share a similar observed property in their shape and velocity span with the foot points of loops 1 and 2, whereas their masses are ~ 10 times larger than the foot points of loops 1 and 2. The larger mass of the two clumps suggests that they are in a later evolutionary stage by a similar argument for loop 3 (Paper II) and/or that they have higher gas density due to their proximity to the CMZ.

4.2. HI

Figure 11 shows a comparison between ^{12}CO and HI where the HI data were taken with the Parkes 64m telescope having a $16'$ beam (McClure-Griffiths et al. 2005). Figures 11a and 11c are for loop 1 and Figures 11b and 11d for loop 2 in the l - b and l - v diagrams. Although there are strong emissions from the foreground disk component ($V_{\text{LSR}} \simeq -50\text{--}0 \text{ km s}^{-1}$) and the 3-kpc arm ($V_{\text{LSR}} \simeq -100\text{--}-50 \text{ km s}^{-1}$) in Figures 11c and d, the HI toward loop 1 shows clear similarity to the CO distributions (Figure 11a). The both foot points of loop 1 are bright in CO as well as in HI. On the other hand, HI of the entire loop 2 is not so clearly recognized as loop 1 due to the contamination, whereas the western half of loop 2 in $(l, b) \simeq (355^\circ\text{--}356^\circ, 1.2^\circ\text{--}2.5^\circ)$ is recognized in HI (Figure 11b). In Figure 11d we find clearly these emissions in $l \simeq 355.3^\circ$ and $V_{\text{LSR}} \simeq -70\text{--}-50 \text{ km s}^{-1}$ and in $l \simeq 356.0^\circ\text{--}357.4^\circ$ and $V_{\text{LSR}} \simeq -170\text{--}-100 \text{ km s}^{-1}$. The inside of

loop 1 shows weak HI emission (Figure 11a), whereas the outside of loops 1 and 2 shows little HI emission. In Figure 12a loop 1 is seen from $V_{LSR} \simeq -150--100 \text{ km s}^{-1}$ as a tilted feature in $b \simeq 0.6^\circ-1.0^\circ$ and HI is associated with this CO feature (Figure 12b). The ^{12}CO features in $b \simeq 0.8^\circ-2.0^\circ$ and $V_{LSR} \simeq -100--40 \text{ km s}^{-1}$ correspond to part of loops 1 and 2, whereas their HI counterparts are not clearly separated from the 3-kpc arm peaked at $V_{LSR} \simeq -60 \text{ km s}^{-1}$.

To summarize, loop 1 and the upper part of loop 2 show HI counterparts as in case of loop 3 (Paper II), although the HI counterpart of the lower part of loop 2 is not clearly identified due to the heavy contamination.

4.3. Dust

In order to test if the loops in CO and HI are seen in the dust emission we have compared dust emission obtained with IRAS at 60 and 100 μm (Miville-Deschênes & Lagache 2005), where we did not use shorter wavelength data because of the possible contamination by the zodiacal light. Figures 13a and 13b show comparison between the total integrated intensity of ^{12}CO from -300 to 300 km s^{-1} , including loops 1, 2 and 3, and IRAS 60 μm and 100 μm emissions, respectively. We find that the enhanced CO emission above $b \simeq 1^\circ$ in a range of $l \simeq 355^\circ-358^\circ$ shows a good coincidence with the dust emissions; the hole of the CO emission at $l \simeq 356.5^\circ$ and the vertical feature at $(l, b) \simeq (355.3^\circ, 1.2^\circ-2.0^\circ)$ are recognized well particularly at 100 μm . We note, however, that the correlation is not seen due to the heavy contamination by the foreground disk emission. Figure 14 shows four panels of CO in different velocity intervals and suggests that both loops 1 and 3 contribute significantly to the main dust emission at b above $\sim 1^\circ$ and $l \simeq 355^\circ-358^\circ$; e.g., the western half of loop 2 at $(l, b) \simeq (355.3^\circ, 1.2^\circ-2.0^\circ)$ shows a clear counterpart in the IRAS emission (Figure 14b). There is another CO feature from the foreground in the same region toward $(l, b) \simeq (355.3^\circ, 1.2-2.0^\circ)$ (Figure 14c) and both loop 2 and the foreground feature possibly contribute to the dust emission here, whereas the peak of the foreground CO emission around $(l, b) \simeq (359.2^\circ, 1.7^\circ)$ shows an offset from the IRAS emission above, suggesting that the loop 2 mainly contribute to the dust emission. Figures 15a and 15b, a comparison between IRAS and the HI, where the IRAS emission is convolved to the same beam size with HI, shows that the dust emissions have similar high- b distribution as in Figure 13. We use the convolved data in the following analysis in Section 5.

5. Mass estimates

Estimating molecular mass in the Galactic center is important in terms of energetics. It is, however, not appropriate to use the virial theorem, if the magnetic flotation (Paper I) is working and if, accordingly, the gas dynamics is far from the dynamical equilibrium. In Paper I the authors estimated a lower limit for the total molecular mass in loops 1 and 2 with ^{13}CO because ^{13}CO observations are confined to $b \leq 1^\circ$. Here we attempt to derive a more accurate value of the total masses of loops 1, 2 and 3 by comparing the ^{12}CO integrated intensity and the

molecular column density derived from both dust emission and HI emission. We use a velocity range from -300 to 300 km s $^{-1}$ for calculating ^{12}CO integrated intensity. We estimate the total hydrogen column densities by including helium atoms of 10 % of total hydrogen atoms.

We used the following relationship to convert the dust emission into the total column density of hydrogen atoms including both of HI and H $_2$, $N(\text{HI})_{\text{dust}}$, by assuming the gas to dust mass ratio, R_{gd} ;

$$N(\text{HI})_{\text{dust}} = \frac{4}{3} \left(\frac{a\rho}{Q_{100}} \right) \frac{\tau_{100} R_{\text{gd}}}{1.4m_{\text{H}}} \text{ (cm}^{-2}\text{)} \quad (1)$$

where a is the grain radius in cm, ρ is the grain density in g cm $^{-3}$, Q_{100} is the grain emissivity at 100 μm , and $1.4m_{\text{H}}$ is the atomic hydrogen mass (g) multiplied by a factor for presence of helium. We use an average value for $(a\rho/Q_{100})$ of $(0.3 \times (10 \times \lambda)^\beta)^{-1}$ at wavelength λ for a mixture of graphite and silicate grains (e.g. Agladze et al. 1996). The optical depth at wavelength λ , τ_λ , is represented as follows;

$$\tau_\lambda = \frac{f_\lambda}{B_\nu(\lambda, T_{\text{dust}})} \quad (2)$$

where f_λ (Jy str $^{-1}$) is flux density at λ (μm), and $B_\nu(\lambda, T_{\text{dust}})$ is Planck function. We estimated dust temperature, T_{dust} (K), by comparing flux densities of 60 μm and 100 μm at each observed point with the following equation;

$$\frac{f_{60}}{f_{100}} = \left(\frac{60}{100} \right)^{-3-\beta} \left[\frac{\exp(hc/\lambda_{100}k_bT_{\text{dust}}) - 1}{\exp(hc/\lambda_{60}k_bT_{\text{dust}}) - 1} \right] \frac{\Omega_{60}}{\Omega_{100}} \quad (3)$$

where h is Planck constant, c is the light speed, k_b is Boltzmann constant and Ω_{60} and Ω_{100} are the solid angles at 60 μm and 100 μm , respectively. We assume that $\Omega_{60} = \Omega_{100}$.

Atomic hydrogen column densities are calculated assuming that the HI 21 cm line is optically thin and spin temperature $T_s(K) \gg h\nu/k$. The following equation is used:

$$N(\text{HI})_{\text{HI}} = 1.82 \times 10^{18} \times W(\text{HI}) = 1.82 \times 10^{18} \int T_{\text{R}}^* dv \text{ (cm}^{-2}\text{)} \quad (4)$$

where $W(\text{HI})$ is HI integrated intensity and T_{R}^* is the HI radiation temperature (K).

We shall take into account that the CO emission integrated in the whole velocity range consists of that in the Galactic center, $W(\text{CO})_{\text{gc}}$, and that from the fore- and background, $W(\text{CO})_{\text{disk}}$. We denote the X-factor in the Galactic center X_{gc} by assuming that loops 1, 2 and 3 at ~ 1 kpc from the center have the same X-factor and $X_0 = 2.0 \times 10^{20}$ cm $^{-2}$ (K km s $^{-1}$) $^{-1}$ as the typical value in the disk (e.g. Strong et al. 1988; Hunter et al. 1997; ?). $W(\text{CO})$ is calculated for a velocity range -300 – 300 km s $^{-1}$ and $W(\text{CO})_{\text{gc}} = W(\text{CO}) - W(\text{CO})_{\text{disk}}$. A comparison between $W(\text{CO})_{\text{gc}}$ and $N(\text{H}_2)$ in the Galactic center is shown in Figure 17b, where the latter is expressed as follows;

$$[N(\text{H}_2) \text{ in the Galactic center}] = W(\text{CO})_{\text{gc}} \times X_{\text{gc}} \quad (5)$$

$$= (N(\text{HI})_{\text{dust}} - N(\text{H})_{\text{HI}})/2 - W(\text{CO})_{\text{disk}} \times X_0 \quad (6)$$

We chose the tops of the loops shown by the two boxes in Figure 15 for this comparison because these regions are not significantly contaminated by the foreground emission and we can clearly distinguish between the disk components and the loops there (Figure 16). Finally, we chose the velocity range of the disk components from -30 to 15 km s $^{-1}$ (gray area in Figure 16) and calculate $W(\text{CO})_{\text{gc}}$ and $W(\text{CO})_{\text{disk}}$. We note here that the contribution of ionized hydrogen is negligibly small because the dust content in the H II regions should become much less than in HI gas due to ultraviolet photons. This is consistent with that the 60 μm and 100 μm emissions are from cold dust grains with dust temperature of ~ 20 – 30 K. We did not take into account the possible contribution of the unknown component that is not detected either in HI or CO, suggested from the γ rays (Grenier, Casandjian & Terrier 2005).

We have here two parameters in the fitting, i.e., β and R_{gd} . In order to simplify the procedure we first fix β to be 2.0 since this index is relatively well established from previous observations (e.g., Draine & Lee 1984). The value of R_{gd} is known to be around 100 in the general ISM but can vary depending on the dust fraction in the gas. We made plots of $W(\text{CO})_{\text{gc}}$ and $N(\text{H}_2)$ in the Galactic center from equation (6) for R_{gd} from 90 to 290 (Figure 17a) and found that the value of the intercept in $N(\text{H}_2)$, the $N(\text{H}_2)$ for $W(\text{CO})_{\text{gc}}=0.0$ K km s $^{-1}$, varies from -20×10^{20} cm $^{-2}$ to 20×10^{20} cm $^{-2}$ in the above range of R_{gd} . We adopt R_{gd} so as that the intercept becomes zero, as is the case if the dust is either in the neutral HI or H $_2$ gas. The best-fit result is shown by the solid regression in Figure 17b. The X-factor and R_{gd} are estimated to be $0.7(\pm 0.1) \times 10^{20}$ cm $^{-2}$ (K km s $^{-1}$) $^{-1}$ and $248(\pm 10)$, respectively. Here we include $\sim 10\%$ error in the 60 μm intensity, $\sim 14\%$ error in the 100 μm intensity (Miville-Deschênes & Lagache 2005) and $\sim 10\%$ error of the CO integrated intensity. The derived X-factor $0.7(\pm 0.1) \times 10^{20}$ cm $^{-2}$ (K km s $^{-1}$) $^{-1}$ agrees well with an X-factor 0.8×10^{20} cm $^{-2}$ (K km s $^{-1}$) $^{-1}$ estimated in the inner Galaxy by comparing the IRAS and gas emission by Bloemen, Deul & Thaddeus (1990) who used the IRAS, CO and HI emissions by adopting a model for dust emissivities as a function of the distance from the Galactic center. If we use X_0 of 1.6×10^{20} cm $^{-2}$ (K km s $^{-1}$) $^{-1}$ (Hunter et al. 1997) for the calculations, R_{gd} and X_{gc} are derived to be 220 and 0.6×10^{20} cm $^{-2}$ (K km s $^{-1}$) $^{-1}$, respectively, fairly similar to the above X_{gc} . The total molecular masses in loops 1, 2 and 3 are estimated to be $\sim 1.2 \times 10^6 M_{\odot}$, $\sim 1.6 \times 10^6 M_{\odot}$ and $\sim 5.5 \times 10^6 M_{\odot}$ with the present X-factor as given in Table 2.

Next, we estimate the molecular mass of the loops with ^{13}CO because there is an uncertainty for mass estimation with optically thick ^{12}CO . We shall extrapolate the mass at $b \geq 1^\circ$ by comparing $W(\text{CO})$ and the molecular column density estimated from ^{13}CO . The optical depth of ^{13}CO , $\tau(^{13}\text{CO})$, was calculated using following equation:

$$\tau(^{13}\text{CO}) = -\ln \left[1 - \frac{T_{\text{R}}^*(^{13}\text{CO})}{5.29 \times (J(T_{\text{ex}}) - 0.164)} \right] \quad (7)$$

where $T_{\text{R}}^*(^{13}\text{CO})$ and T_{ex} are the peak radiation temperature (K) and the excitation temperature (K) of ^{13}CO , respectively. $J(T)$ is defined as $J(T) = 1/[\exp(5.29/T) - 1]$. ^{13}CO column density

$N(^{13}\text{CO})$ (cm^{-2}) was estimated from:

$$N(^{13}\text{CO}) = 2.42 \times 10^{14} \frac{\tau(^{13}\text{CO})\Delta VT_{\text{ex}}}{1 - \exp(-5.29/T_{\text{ex}})} \quad (\text{cm}^{-2}) \quad (8)$$

where ΔV is the ^{13}CO linewidth in km s^{-1} . $N(^{13}\text{CO})$ is calculated for each position which matches the observed position in ^{12}CO . In this study, we assume T_{ex} of 40 K and two abundance ratio from ^{13}CO to H_2 , $[\text{H}_2]/[^{13}\text{CO}]$, of 5×10^5 (Dickman 1978) and 1×10^6 (Lis & Goldsmith 1989). The comparison between $W(\text{CO})$ and $N(\text{H}_2)$ is shown in Figure 18. The conversion functions for loops 1 and 2 and loop 3 are estimated as $N(\text{H}_2) = [1.1(\pm 0.2) \times 10^{20}W(\text{CO}) - 4.1(\pm 3.0) \times 10^{21}]$ (cm^{-2}) and $N(\text{H}_2) = [1.6(\pm 0.3) \times 10^{20}W(\text{CO}) - 1.1(\pm 0.5) \times 10^{22}]$ (cm^{-2}), respectively. If we use $[\text{H}_2]/[^{13}\text{CO}]$ of 1×10^6 (Lis & Goldsmith 1989), derived $N(\text{H}_2)$ is doubled. Then we calculate the total molecular masses of loops 1, 2 and 3 including $b \geq 1.0^\circ$ as $\sim(0.8-1.6) \times 10^6 M_\odot$, $\sim(1.5-3.0) \times 10^6 M_\odot$ and $\sim(6.0-12.0) \times 10^6 M_\odot$, respectively, consistent with the molecular mass estimated for the present X-factor. Here negative solutions of $N(\text{H}_2)$ are neglected.

The atomic mass of loop 1 was estimated to be $\sim 2.4 \times 10^5 M_\odot$, including the mass of $\sim 0.7 \times 10^5 M_\odot$ inside of the loop, $(l, b) \simeq (356.4^\circ-357.2^\circ, 0.6^\circ-1.0^\circ)$, and that of loop 2 is estimated to be $\sim 2.5 \times 10^5 M_\odot$ for $(l, b) \simeq (355.0^\circ-356.0^\circ, 1.2^\circ-2.5^\circ)$, by using equation (4). The loop 2 HI mass is a lower limit since the lower half is not included. Then, the total gas mass of loops 1 and 2 are estimated to be $\sim 1.4 \times 10^6 M_\odot$ and $\sim 1.9 \times 10^6 M_\odot$, respectively. We also estimate the mass of the foot points to be $(1-6) \times 10^5 M_\odot$ for each. If we assume a uniform velocity dispersion of 20 km s^{-1} in the loops, the total kinetic energy of each loop amounts to $\sim(1-6) \times 10^{52}$ erg.

6. Geometry and kinematics of the loops

Paper II derived the geometrical and kinematic properties of loop 3 by assuming a constant radius. We shall here estimate the geometrical and kinematical parameters of loops 1 and 2 such as radius, rotation and radial velocities following Paper II with small modifications.

First, we estimate the geometrical parameters of the loops. For simplicity we assume that the two loops have the same radius, physical length and shape and subtend the same angle with respect to the center. By considering triangles the corners of which are the Galactic center, the Sun, and a foot point of loops (the left foot point of loop 1: $l_0 \simeq 357.5^\circ$, the right foot point of loop 1 and the left foot point of loop 2: $l_1 \simeq 356.0^\circ$, and the right foot point of loop 2: $l_2 \simeq 355.5^\circ$), we can derive simultaneous equations by applying sine theorem to the three triangles;

$$R = \frac{R_0 \sin l_0}{\sin(\theta_0 + l_0)} \quad (9)$$

$$R = \frac{R_0 \sin(l_1)}{\sin(\theta_0 + \theta + l_1)} \quad (10)$$

$$R = \frac{R_0 \sin(l_2)}{\sin(\theta_0 + 2\theta + l_2)} \quad (11)$$

where R is the radius, R_0 is the distance to the Galactic center, 8.5 kpc, θ is the angles subtended by the arcs between the foot points at the Galactic center and θ_0 is an offset. A schematic view of these parameters are shown in Figure 19. We then solve the equations and derive R , θ_0 , and θ as ~ 670 pc, $\sim 27.5^\circ$, and $\sim 31^\circ$, respectively. Therefore, the location of the left end of loop 1 is at $\theta_0 \simeq 27.5^\circ$, the right end of loop 1 and the left end of loop 2 is at $\theta_0 + \theta \simeq 58.5^\circ$, and the right end of loop 2 is at $\theta_0 + 2\theta \simeq 89.5^\circ$. The projected length to the disk of each loop, L , is 360 pc.

Next, we estimate the kinematical parameters of the loops. It is uncertain if the loops have radial motions. Some other features like the expanding molecular ring (EMR) are supposed to be expanding (Sawada et al. 2001; Morris & Serabyn 1996). We shall for simplicity assume that the loops are rotating and expanding from the center although the expansion is not yet confirmed in loops 1 and 2. All the molecular gas of loops 1 and 2 has negative velocities. The velocity with respect to the LSR, V_{LSR} , is then expressed as follows;

$$V_{\text{LSR}} = V_{\text{rot}} \frac{R_0}{R} \sin l - V_{\text{exp}} \left(1 - \frac{R_0^2}{R^2} \sin^2 l \right)^{\frac{1}{2}} - V_{\text{sun}} \sin l \quad (12)$$

where V_{rot} is the rotational velocity of the disk, V_{exp} is the expansion velocity, and V_{sun} is the rotation velocity of the LSR about the center ~ 200 km s $^{-1}$. We estimate that V_{exp} is ~ 141 km s $^{-1}$ and V_{rot} is ~ 47 km s $^{-1}$. These parameters are listed in Table 3 for the three loops, and Figure 19 shows a schematic face-on view of these loops. The radius of loops 1 and 2 is somewhat smaller than that of loop 3.

7. Discussion

We shall here discuss the loops along the line of the Parker instability following Paper I and shall not repeat discussion on the other possibilities including supershells (Papers I and II).

7.1. Magnetic flotation theory and its application to the loops

Parker (1966) presented the pioneering work on the Parker instability in order to explain cloud formation in the foot point of a magnetic loop in the Galaxy. Horiuchi et al. (1988) and Matsumoto et al. (1988) made detailed studies of the Parker instability analytically with a linear analysis and numerically including nonlinearity. Their results indicate that the fundamental parameters are the Alfvén speed $V_A = B/\sqrt{4\pi\rho}$ and the pressure scale height H , where B is the magnetic field and ρ is the gas density. The height and length of a loop is given as a few times H and several times H , respectively. A typical timescale is given by the ratio H/V_A . A reasonable scenario is that the differential rotation in the nuclear disk creates toroidal magnetic field where the molecular gas is frozen-in to the field lines; the molecular gas in the disk is ionized at an

ionization degree of $\sim 10^{-7}$ by cosmic ray protons and the ionization degree is high enough for the frozen-in condition (e.g., Güsten & Philipp 2004). Indirect arguments on the arched filaments suggest that the field strength is as large as ~ 1 mG (Yusef-Zadeh & Morris 1987), ~ 1000 times larger than the typical field strength of $\sim \mu\text{G}$ in the disk, whereas the field strength may be much less in lower density regions (LaRosa et al. 2006). The magneto-hydrodynamics (MHD) describes well the gas disk. The mG field is a natural outcome of the gravitational potential in the central few 100 pc that is more than few 100 times deeper than in the disk. An outstanding observational property of a magnetic flotation loop is that the falling down gas becomes often supersonic and forms shock fronts in the both ends of the loop, where gas density and velocity dispersion become enhanced (Matsumoto et al. 1988). These compressed regions appear as foot points of enhanced density. This supersonic motion and heating indicate that magnetic flotation may explain the origin of high temperature and violent motion in the Galactic center (Paper I).

Three molecular loops, loops 1, 2 and 3, were discovered in the Galactic center and an interpretation was presented that they are created by the Parker instability in the magnetized nuclear disk with a field strength of $\sim 150 \mu\text{G}$ (Papers I, II). The three loops show sizes consistent with the above theoretical predictions for a scale height of ~ 100 pc in the central several 100 pc. They also show foot points on their both ends and the gas in the foot points appears heated and compressed by the shock fronts. For a strong field of $100 \mu\text{G}$ and gas density of 100 cm^{-3} , the Alfvén speed is a few 10 km s^{-1} and the flotation time scale becomes a few Myrs for a 100 pc scale height. An LVG analysis of the CO $J=1-0$, $3-2$, and $4-3$ transitions indicates that the typical gas temperature is about $\sim 30-50$ K or more in the foot points of loops 1 and 2, whereas no stellar heat source is found there (Torii et al. 2010). These are reasonable properties of the foot points in the magnetic flotation. We note that another remarkable aspect of the loops is the spur, a vertical upward flow of gas above the foot point reaching a height more than the loop height. The present velocity channel distributions show evidence for such a spur in two places, offering additional pieces of evidence that support the magnetic flotation picture.

Generally, it is easier for lower density gas to be lifted up rather than for dense molecular gas by the magnetic flotation and it might seem odd that the dense molecular gas forms the loops. In order to reproduce the observed cool molecular loops in the Galactic center Takahashi et al. (2009) have carried out two-dimensional numerical simulations for part of the disk containing the equatorial plane by adopting a stratified disk having three layers; cool layer ($T \simeq 10^3$ K), warm layer ($T \simeq 10^4$ K), and hot layer ($T \simeq 10^5$ K). It is important to note that their calculations produced a top-heavy loop which shows a higher density layer in the top. This is because the loop in the cool layer has initially a small curvature, making the loop top flat, and the flat-top loop continuously rises to efficiently accumulate the gas around the loop top. Loop 1 shows that the higher density CO gas covers the lower density HI inside the CO loop (see Figure 11), indicating that the observations are well reproduced by the local numerical

simulations by Takahashi et al. (2009). Higher resolution HI observations may shed light on this rising HI. It is shown by the TRACE satellite at UV that such continuous rising loops are actually observed in the sun.

We also note that the ambient HI gas may be being converted into H₂ during the flotation. The shock compression by the rising loop in the upper part may lead to form molecular gas along the loop which is initially atomic. It is likely that the loop is surrounded by HI gas and the motion of the flotation at V_A inevitably causes shocks in the front side. This can lead to form H₂ in the shock compressed layer along the loop. The time scale of H₂ formation is given as $10^9/n(\text{H})$ yrs, where $n(\text{H})$ is the number density of HI gas in cm^{-3} (Spitzer 1978), and is estimated to be ~ 10 Myrs for $n(\text{H})$ of 100 cm^{-3} . This time scale is consistent with the present ratio H/V_A .

A global aspect of the loops on a kpc scale is also to be compared between theories and observations. Machida et al. (2009) carried out three-dimensional global numerical simulations of the nuclear gas disk and showed that the magneto-rotational instability coupled with the Parker instability works to create many loops over a 2 kpc-radius nuclear disk, where the axially symmetric Miyamoto-Nagai potential (Miyamoto & Nagai 1975) was adopted as the stellar gravitational field. Machida et al. (2009) have shown that one-armed non-axisymmetric density pattern of $m = 1$ mode is developed in the nuclear disk. In half of the azimuthal area of the nuclear disk having lower density, magnetic pressure tends to become stronger compared with gas pressure and prominent magnetic loops are formed preferentially on this side of the disk rather than in the other half having higher density. Such predicted asymmetry of the global distribution of the loops generally seems to be consistent with the observations that about three-fourths of the dense molecular gas, the CMZ, is distributed in the positive Galactic longitude and that three loops are distributed in the negative Galactic longitude. We note that Clump 2 and the $l = 5.5^\circ$ complex are located outside the CMZ where the surface gas density is lower than in the CMZ but is yet higher than in the negative longitude side where loops 1–3 are distributed. This is consistent with the global simulations.

The bar-like gravitational potential is considered to be a viable mechanism to explain the radial motions of the gas in the central few 100 pc of the Galaxy (Binney et al. 1991, see also Liszt 2006). In order to incorporate the effects of the bar-like potential, it is required to develop a model which adopts the bar potential instead of the Miyamoto-Nagai potential in the global simulations of the magnetized gas disk. It is naturally expected that magnetic flotation loops are also created in such calculations because the basic physics remains the same in connection with the Parker instability.

7.2. Comparisons with the Solar phenomena

The present study revealed helical distributions of the loops. On the solar surface we find similar helical distributions which may be explained by MHD instabilities. Figures 8 and 9

reveal that loops 1 and 2 have helical distributions which change within a small velocity interval of $\sim 4 \text{ km s}^{-1}$. We shall compare these distributions with solar loops and theoretical calculations of magneto-hydrodynamics and discuss formation mechanisms of the helical distributions.

First, we attempted to estimate the amplitude and wavelengths of the helix by applying sinusoidal and elliptical functions as follows;

$$\left(\frac{(l - l_c) - A \sin(k\Theta + \Delta\Theta) \cos \Theta}{X}\right)^2 + \left(\frac{(b - b_c) - A \sin(k\Theta + \Delta\Theta) \sin \Theta}{Y}\right)^2 = 1 \quad (13)$$

where l_c and b_c are the central position of an ellipse, a and b are the semi-major and semi-minor of the ellipse, A is the wave amplitude, k is the wave number in the ellipse, Θ is defined as $\Theta = \arctan(Y(l - l_c)/X(b - b_c))$ and $\Delta\Theta$ is an offset of Θ . As a result we find the parameters in Table 4 show reasonable fits to the observations as shown in Figures 8 and 9. The wavelengths of helix in loops 1 and 2 are estimated to be $\sim 0.28^\circ$ (41 pc)– 0.42° (62 pc) and $\sim 0.28^\circ$ (41 pc), and the amplitudes are estimated $\sim 0.2^\circ$ (29 pc)– 0.34° (50 pc) and $\sim 0.26^\circ$ (38 pc), respectively.

Next we compare the above results with the solar phenomena. It has been known that solar prominences show helical distributions (e.g., Matsumoto et al. 1998). Formation of prominences are discussed under the following two ideas; 1) Magnetic flux tubes having helical shapes originally rise up, and 2) Magnetic reconnection in the corona forms a helical shape. Recent Hinode observations show evidence for 1) (Okamoto et al. 2008) and we shall discuss possibility of formation of the distorted field in the disk. One possible candidate along this line is the shear effect. A gas disk rotating differentially drives the magneto-rotational instability (MRI, Balbus & Hawley 1991) due to the shear motion. MRI drives magnetic turbulence inside the disk (e.g. Hawley et al. 1995; Matsumoto & Tajima 1995) and distorted fields are formed.

Another possibility including 2) is discussed by Shibata & Matsumoto (1991). They suggested that floating loops driven by the Parker instability could be affected by Coriolis force and the loops are twisted. Then the twisted fields are accumulated in the foot points of the loops by falling motion of gas.

In addition, Matsumoto et al. (1998) showed that distorted magnetic field lines becoming unstable against the kink instability form a helical shape while they rise. Hood & Priest (1981) give a condition of the kink instability as the number of turns in the helical distributions in a loop $\Phi > 2.5$. Observed helical distributions in loops 1 and 2 are estimated to be $\sim 3\pi$ and $\sim 5\pi$, respectively, satisfying the requirement.

The present findings of the helical distributions in loops 1 and 2 offers a support for that the magnetic floatation is a viable idea to explain these features and more detailed numerical simulations are desirable in this direction.

8. Summary

We have presented a detailed study of molecular loops 1 and 2 in the Galactic center based on the NANTEN ^{12}CO and $^{13}\text{CO}(J=1-0)$ dataset. The main conclusions are summarized below;

1) A full account of the ^{12}CO dataset at 10 pc resolution obtained with the NANTEN 4m telescope is presented mainly in velocity channel distributions every 10 km s^{-1} from -180 to 20 km s^{-1} for an area $(l, b) \simeq (355.0^\circ-359.0^\circ, -1.0^\circ-2.5^\circ)$. For part of the area, the ^{13}CO distribution is also presented. We newly identified helical distributions in the tops of loops 1 and 2, an unusual small loop-like feature in the western foot point of loop 2 and two spurs above the foot points.

2) We compared the foot points of loops 1 and 2 with the known two broad molecular features Clump 2 and the $l = 5.5^\circ$ complex and found that they share common properties; the elongation vertical to the plane with a size of $\sim 30 \text{ pc} \times \sim 100 \text{ pc}$ and large velocity spans of $50-150 \text{ km s}^{-1}$, suggesting that they may be of a similar origin. Most of them have $\sim 10^5-10^6 M_\odot$, whereas Clump 2 is the most massive one of $\sim 10^6 M_\odot$.

3) A comparison with the HI emission indicates that loops 1 and 2 have atomic components, while the atomic component in the lower part of loop 2 is not seen due to heavy contamination by the foreground features. The mass fraction of the atomic component is 10-20% of the molecular component, indicating that the atomic gas is a minor component in the loops.

4) A comparison with the dust emission at $60 \mu\text{m}$ and $100 \mu\text{m}$ shows that the loops 1, 2 and 3 are associated with the dust features at b higher than 1.0° , whereas the association is not clear at b lower than 1.0° due to the contamination. Based on the good correlation among CO, HI and dust, we derived an X-factor for the central kpc to convert the ^{12}CO intensity to molecular hydrogen column density to be $0.7(\pm 0.1) \times 10^{20} \text{ cm}^{-2} (\text{K km s}^{-1})^{-1}$.

5) The total mass of loops 1 and 2 are estimated to be $\sim (1.4-1.9) \times 10^6 M_\odot$. The total kinetic energy of loops 1 and 2 are estimated to be $\sim 10^{52}$ ergs for the observed velocity dispersions.

6) By assuming that the two loops are of the same size at a radius R from the center, we estimate the geometrical and kinematical properties of the loops; the projected length of a loop, L , the angle subtended by a loop, θ , and the rotation and expansion velocities, V_{rot} and V_{exp} . The results are as follow; $R \simeq 670 \text{ pc}$, $L \simeq 360 \text{ pc}$, $\theta \simeq 31^\circ$, $V_{\text{rot}} \simeq 47 \text{ km s}^{-1}$ and $V_{\text{exp}} \simeq 141 \text{ km s}^{-1}$.

7) Recent theoretical works both in global 3-dimensional and local 2-dimensional on magnetically flotation loops (Machida et al. 2009, Takahashi et al. 2009) are compared with the observations and we confirmed that the theoretical results are consistent with the observational properties of the two loops. The helical distributions in the loop tops are compared with similar

solar features and we found that the basic parameters of a helical distribution are explained in terms of magnetic effects.

We greatly appreciate the hospitality of all staff members of the Las Campanas Observatory of the Carnegie Institution of Washington. The NANTEN telescope was operated based on a mutual agreement between Nagoya University and the Carnegie Institution of Washington. We also acknowledge that the operation of NANTEN can be realized by contributions from many Japanese public donators and companies. This work is financially supported in part by a Grant-in-Aid for Scientific Research (KAKENHI) from the Ministry of Education, Culture, Sports, Science and Technology of Japan (Nos. 15071203 and 18026004) and from JSPS (Nos. 14102003, 20244014, and 18684003). This work is also financially supported in part by core-to-core program of a Grant-in-Aid for Scientific Research from the Ministry of Education, Culture, Sports, Science and Technology of Japan (No. 17004) and by the Global COE Program of Nagoya University gQuest for Fundamental Principles in the Universe (QFPU)h from JSPS and MEXT of Japan.

References

- Agladze, N. I., Sievers, A. J., Jones, S. A., Burlitch, J. M., Beckwith, S. V. W. 1006, *ApJ*, 462, 1026
- Balbus, S. A. & Hawley, J. F. 1991, *ApJ*, 376, 214
- Bania, T. M. 1977, *ApJ*, 216, 381
- Binney, J., Gerhard, O. E., Stark, A. A., Bally, J., & Uchida, K. I. 1991, *MNRAS*, 252, 210
- Bitran, M., Alvarez, H., Bronfman, L., May, J., & Thaddeus, P. 1997, *A&AS*, 125, 99
- Bloemen, J. B. G. M., Deul, E. R. & Thaddeus, P. 1990, *A&A*, 233, 437
- Boyce, P. J. & Cohen, R. J. 1994, *A&AS*, 107, 563
- Crocker, R. M., Jones, D. I., Melia, F., Ott, J., Protheroe, R. J. 2010, *Nature*, 463, 65
- Dickman, R. L. 1978, *ApJS*, 37, 407
- Draine, B. T. & Lee, H. M. 1984, *ApJ*, 285, 89
- Fujishita, M. et al. 2009, *PASJ*, 61, 1039
- Fukui, Y., Iguchi, T., Kaifu, N., Chikada, Y., Morimoto, M., Nagane, K., Miyazawa, W., Miyaji, T. 1977, *PASJ*, 29, 643D
- Fukui, Y., et al. 2006, *Science*, 314, 106
- Grenier, I. A., Casandjian, J. & Terrier, R. 2005, *Science*, 307, 1292
- Güsten, R., & Henkel, C. 1983, *A&A*, 136-145
- Güsten, R., & Philipp, S. D. 2004, in *Proc. the Fourth Cologne-Bonn-Zermatt Symposium* ed. S. Pfalzner, C. Kramer, C. Staubmeier, A. Heithausen (Heidelberg: Springer), 253
- Hawley, J. F., Gammie, C. F. & Balbus, S. A. 1995, *ApJ*, 440, 742
- Hüttemeister, S., Wilson, T. L., Bania, T. M., & Martín-Pintado, J. 1993, *A&A*, 280, 255
- Hood, A. W., Priest, E. R. 1981, *Sol. Phys.*, 73, 289
- Horiuchi, T., Matsumoto, R., Hanawa, T., & Shibata, K. 1988, *PASJ*, 40, 147
- Hunter, S. D., et al. 1997, *ApJ*, 481, 205
- Lis, D. C., & Goldsmith, P. F. 1989, *ApJ*, 337, 704
- Liszt, H. S. 2006, *A&A*, 447, 533
- Liszt, H. S. 2008, *A&A*, 486, 467
- LaRosa, T. N., Shore, S. N., Joseph, T., Lazio, W., Kassim, N. 2006, *Journal of Physics Conference Series*, 51, 10
- Machida, M. et al. 2009, accepted to *PASJ*
- Martin, C. L., Walsh, W. M., Xiao, K., Lane, A. P., Walker, C. K., & Stark, A. A. 2004, *ApJS*, 150, 239
- Matsumoto, R., Horiuchi, T., Shibata, K., & Hanawa, T. 1988, *PASJ*, 40, 171
- Matsumoto, R. & Tajima, T. 1995, *ApJ*, 445, 767
- Matsumoto, R., Tajima, T., Chou, W., Okubo, A., Shibata, K. 1998, *ApJ*, 493L, 43
- McClure-Griffiths, N. M., Dickey, J. M., Gaensler, B. M., Green, A. J., Haverkorn, N., & Strasser, S. 2005, *ApJS*, 158, 178
- Miville-Deschênes, M. & Lagache, G. 2005, *ApJS*, 157, 302
- Miyamoto, M., & Nagai, R. 1975, *PASJ*, 27, 533
- Morris, M., & Serabyn, E. 1996, *ARA&A*, 34, 645
- Morris, M., Uchida, K., & Do, T. 2006, *Nature*, 440, 308

- Nagai, M., Tanaka, K., Kamegai, K., Oka, T. 2007, PASJ, 59, 25
- Ogawa, H., Mizuno, A., Hoko, H., Ishikawa, H., & Fukui, Y. 1990, Int. J. Infrared Millimeter Waves, 11, 717
- Oka, T., Nagai, M., Kamegai, K., Tanaka, K., & Kuboi, N. 2007, PASJ, 59, 15
- Oka, T., Geballe, T. R., Goto, M., Usuda, T., & McCall, B. J. 2005, ApJ, 632, 882
- Okamoto, T. J. et al. 2008, ApJ, 673L, 215O
- Parker, E. N. 1966, ApJ, 145, 811P
- Rodríguez-Fernández, N. J., Martín-Pintado, J., Fuente, A., de Vicente, P., Wilson, T. L., & Hüttemeister, S. 2001, A&A, 365, 174
- Sawada, T. et al. 2001, ApJS, 136, 189S
- Scoville, N. Z., Solomon, P. M. & Penzias, A. A. 1975, ApJ, 201, 352
- Shibata, K., Matsumoto, R. 1991, Nature, 353, 633S
- Spitzer, L. 1978, Physical processes in the interstellar medium (New York Wiley-Interscience, 1978),123
- Stark, A. A., Bania, T. M. 1986, ApJ, 306, 17
- Strong, A. W. et al. 1988, A&A, 207, 1
- Strong, A. W., Mattox, J. R. 1996, A&A, 308, 21
- Torii, K. et al. 2010, PASJ, 62,675
- Yusef-Zadeh, F., Hewitt, J. W., & Cotton, W. 2004, ApJ, 155, 421
- Yusef-Zadeh, F., Morris, M., & Chance, D. 1984, Nature, 310, 557
- Yusef-Zadeh, F., Morris, M. 1987, AJ, 94, 1178
- Takahashi, K. et al. 2009, submitted to PASJ

Table 1: Summary of the observations

transition	frequency	beamsize	grid	observing region		total observed points	mean r.m.s. (K)
	(GHz)	(')	(')	l (°)	b (°)		
$^{12}\text{CO}(J=1-0)$	115.27120	2.6	4	350–10	–5–5	54000	0.3
$^{13}\text{CO}(J=1-0)$	110.20137	2.6	2	354–8	–1–1	25200	0.2

Table 2: Comparison between the loops and loop candidates

No.	Name	l, b (°, °)	V_{LSR} (km s $^{-1}$)	Size (pc×pc)	M ($10^5 M_{\odot}$)	λ (pc)	H (pc)	M_{tot} ($10^5 M_{\odot}$)	$\frac{M_{\text{fp}}}{M_{\text{tot}}}$
1	loop 1W [†]	356.20, 0.87 [†]	–130–40 [†]	85×100 [†]	6.3 [†]	180	150–180	11.5	0.35
	loop 1E	357.40, 0.73	–180–120	40×50	0.9				
2	loop 2W	355.47, 0.80	–90–40	30×45	2.2	110	240–310	15.7	
	loop 2E [†]	356.20, 0.87 [†]	–130–40 [†]	85×100 [†]	6.3 [†]				
3	loop 3W	355.50, 0.70	45–100	65×75	6.0	420	30–210	55.4	0.16
	loop 3E	358.34, 0.80	70–110	90×100	2.6				
	Clump 2	3.10, 0.17	30–180	75×135	63.3	350	60–160	117.5	0.70
	$l=5.5^{\circ}$ complex	5.47, –0.30	30–170	50×100	19.2				

[†] Loop 1W and loop 2E are argued together because it is difficult to estimate separately.

Note. - Column (1): loop number (2): Name of the foot point. (3): position of the peak integrated intensity region. (4): Velocity range. (5): Size of the foot point (Longitude × Latitude). (6): Molecular mass of the foot point. We used the X-factor of 0.7×10^{20} cm $^{-2}$ (K km s $^{-1}$) $^{-1}$ derived in the text. (7): Projected length between the two foot points. (7): Height of the loop from $b = 0^{\circ}$. (8): Total molecular mass in the loop (including the foot points and the loop top). (8) Mass raatio between the total mass and the foot point masses.

Table 3: Geometrical and kinematical parameters of loops 1 and 2

Name	R (pc)	L (pc)	θ_0 (°)	θ (°)	V_{rot} (km s $^{-1}$)	V_{exp} (km s $^{-1}$)
loops 1 & 2	670	360	28	31	47	141
loop3	1000	750	130	43	80	130

Table 4: Fitted parameters of helixes in loops 1 and 2

Name	l_c (°)	b_c (°)	X (°)	Y (°)	A (°)	k	$\Delta\Theta$ (rad.)
loop 1 [†]	353.40/353.40	0.55/0.47	4.0/4.0	1.7/1.7	0.17/0.10	30/24	0/0
loop 2	356.66	–0.01	0.65	1.92	0.13	17	0.1

[†] loop 1 shows two solutions.

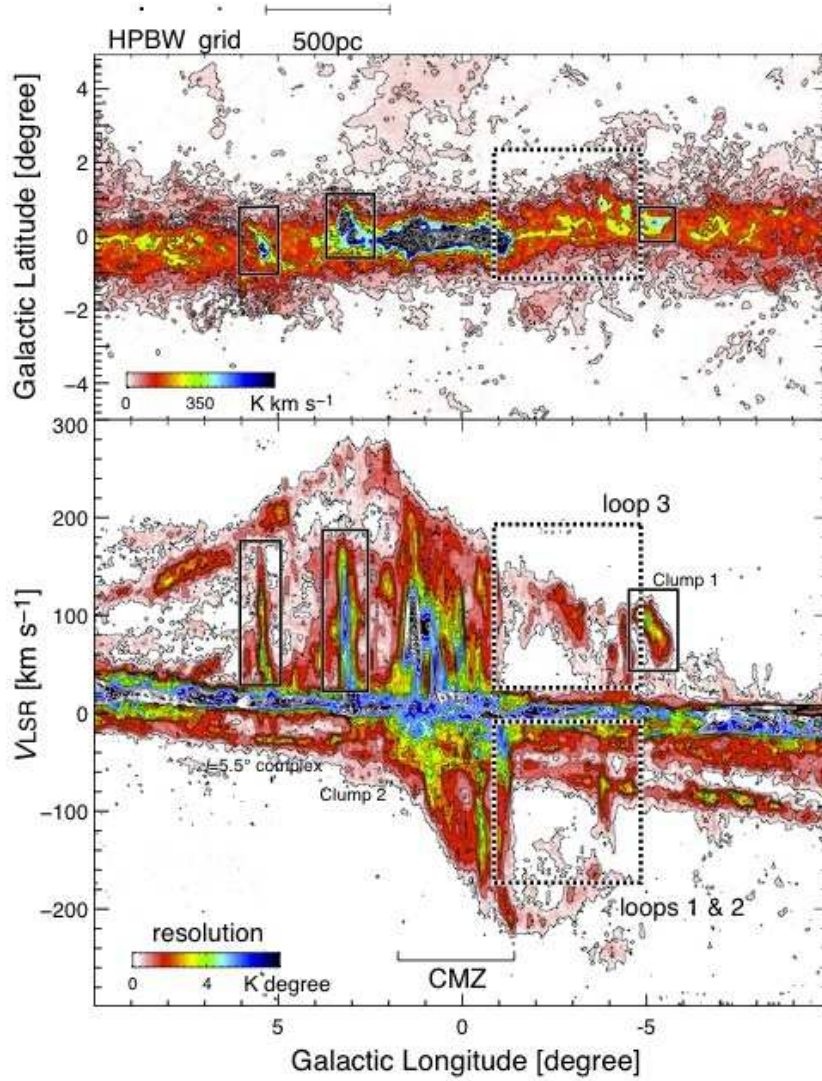


Fig. 1: Integrated intensity distributions of $^{12}\text{CO}(J=1-0)$ obtained by NANTEN. Dotted boxes in the figures show the regions that loops are located. Solid boxes show other broad line features; Clumps 1 and 2 and $l=5.5^\circ$ complex. (a) Velocity integrated intensity distributions. Integration range in velocity is from -300 to 300 km s^{-1} . Contours are plotted at 10, 20, 60, 100, 220, 340 K km s^{-1} in black and 460, 820, 1180, 1540, 1900, 2260, 2620 K km s^{-1} in white. (b) Longitude-velocity diagram. Velocity resolutions are smoothed to 3 km s^{-1} . Integrated range in galactic latitude is from -2° to 2° . Contours are plotted every 6 K degree from 0.25 K degree (black) and then every 1.2 K degree from 10 the one.

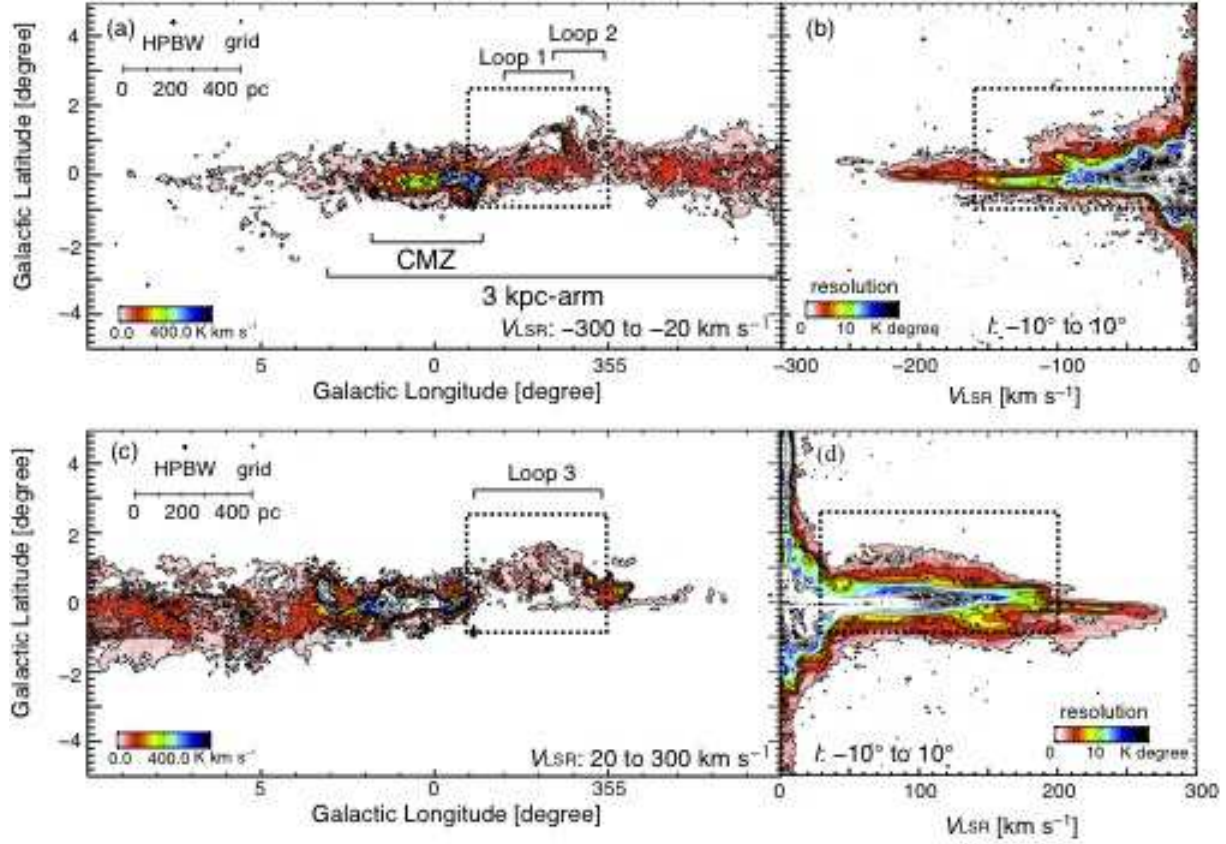


Fig. 2: (a, b) Integrated intensity distributions of loops 1 and 2 in the Galactic center. Dotted boxes show the region that loops 1, 2 and 3 are located. (a) Velocity integrated intensity distributions. Integration range in velocity is from -300 to -20 km s^{-1} . Contours are plotted at 10, 20, 60, 100, 220, 340 K km s^{-1} in black and 460, 820, 1180, 1540, 1900 K km s^{-1} in white. (b) Velocity-latitude diagram. Velocity resolutions are smoothed to 3 km s^{-1} . Integration range in galactic longitude is from -10° to 10° . Contours are plotted every 1.6 K degree from 0.8 K degree (black) and then every 3.2 K degree from 6th one (white). (c, d) Integrated intensity distributions of loop 3 in the Galactic center. Dotted boxes show the region that loop is located. (c) Velocity integrated intensity distributions. Integration range in velocity is from 20 to 300 km s^{-1} . Contours are plotted at the same levels of figure (a). (d) Velocity - latitude diagram. Velocity resolutions are smoothed to 3 km s^{-1} . Integration range in galactic longitude is from -10° to 10° . Contours are plotted at the same levels of figure (b).

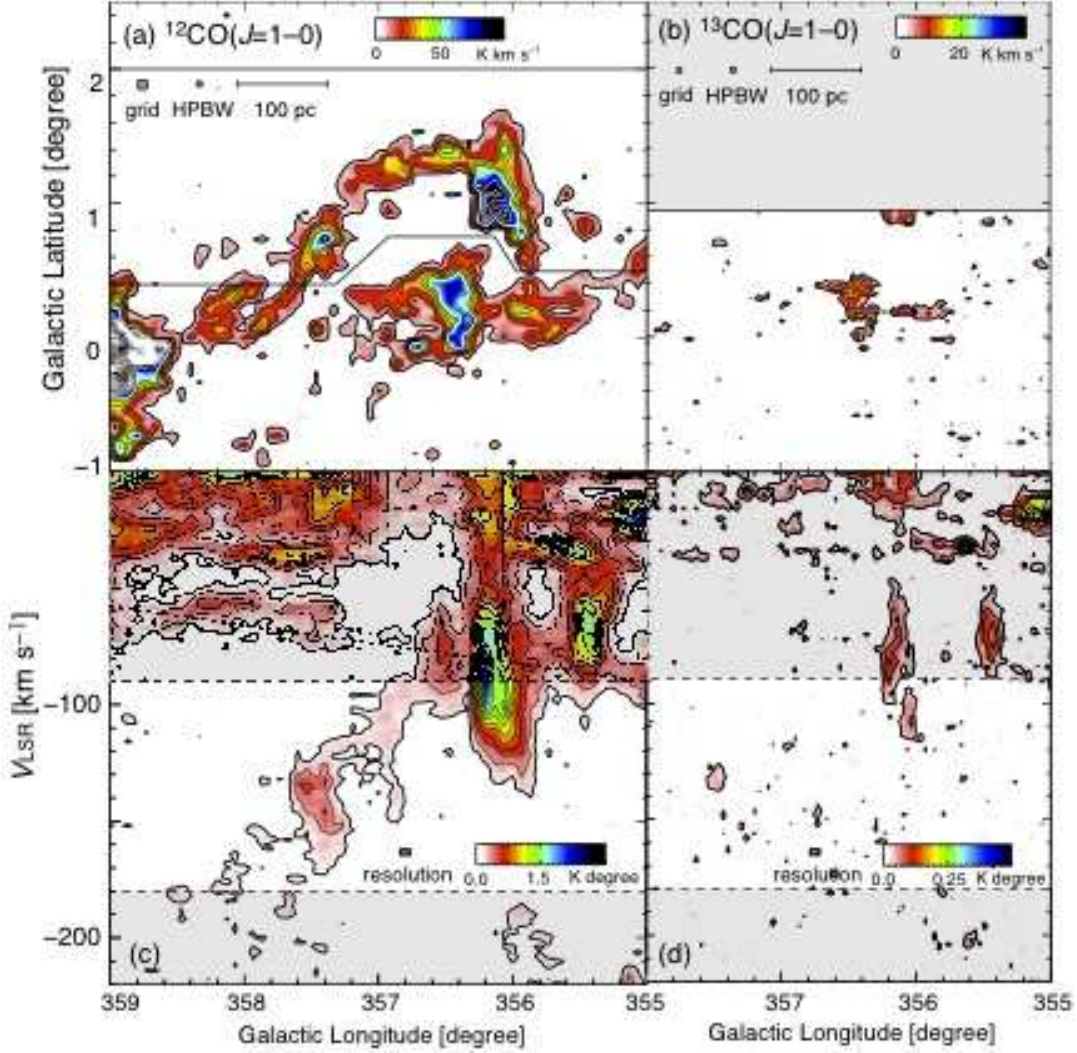


Fig. 3: (a–d) Integrated intensity maps of loop 1 in $^{12}\text{CO}(J=1-0)$ and $^{13}\text{CO}(J=1-0)$. (a) Integrated intensity distributions of loop 1 in $^{12}\text{CO}(J=1-0)$. The integration range in velocity is from -180 to -90 km s^{-1} . Contours are plotted every 10 K km s^{-1} (black line) from the lowest one of 7.0 K km s^{-1} (3σ) and every 20 K km s^{-1} (white line) from the 6th one. (b) Integrated intensity distributions in $^{13}\text{CO}(J=1-0)$. The integration range is the same in the figure (a). Contours are plotted every 4 K km s^{-1} from 3.5 K km s^{-1} . (c) Velocity-galactic longitude diagram of loop 1. The velocity was smoothed at a resolution of 2.0 km s^{-1} . The integration range in the galactic latitude is shown by the solid lines in the figure (a). Contours are plotted every 0.12 K deg from the lowest one of 0.20 K deg . An approximate position of the 3 kpc arm is indicated by a dotted line. (d) Velocity-galactic longitude diagram of loop 2. The velocity is smoothed at a resolution of 2.0 km s^{-1} . The integration range is the same as figure (c). Contours are plotted every 0.05 K deg from 0.035 K deg .

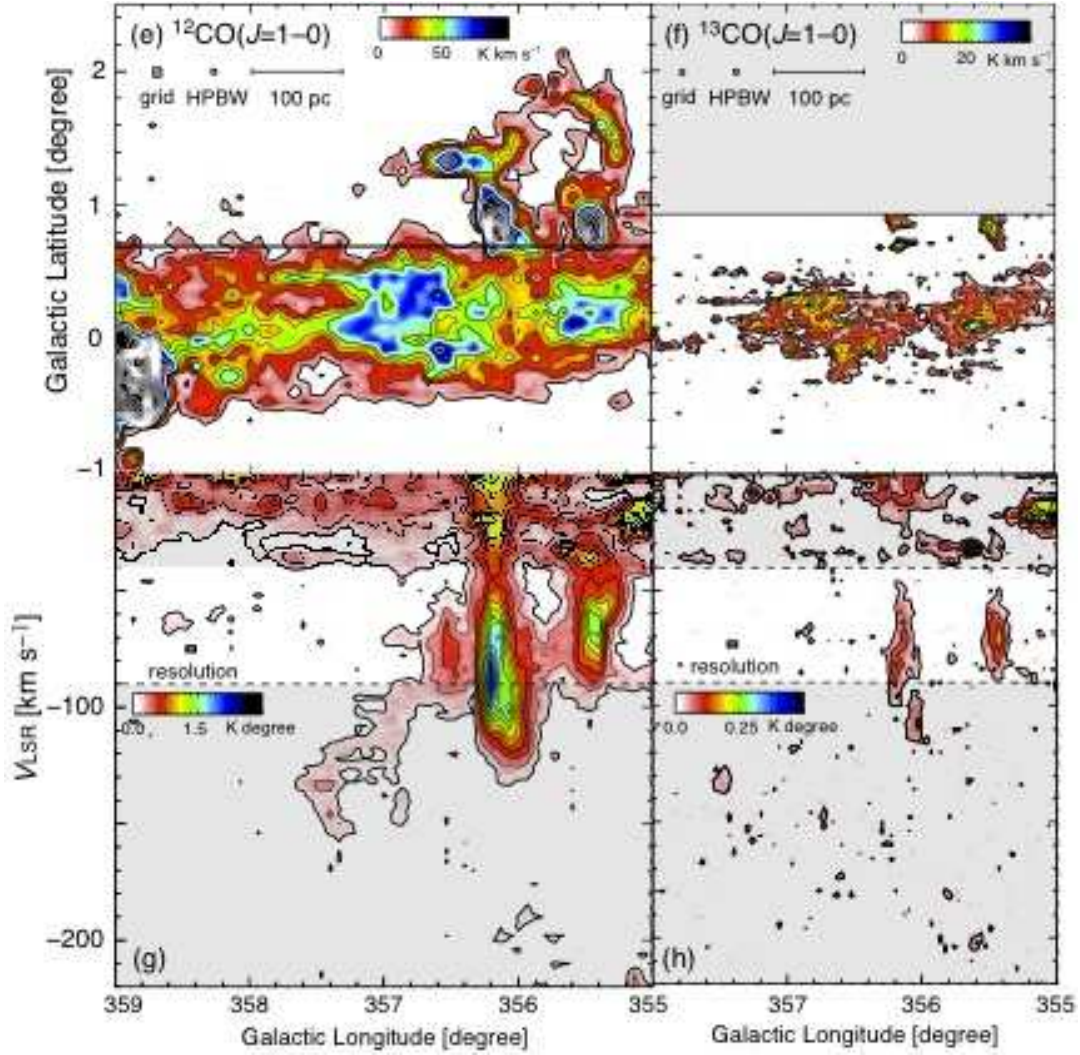


Fig. 3: (e–h) Integrated intensity distributions of loop 2 in $^{12}\text{CO}(J=1-0)$ and $^{13}\text{CO}(J=1-0)$. (e) Position-position diagram of loop 1 in $^{12}\text{CO}(J=1-0)$. The integration range in velocity is from -90 to -40 km s^{-1} . Contours are plotted every 10 K km s^{-1} (black line) from the lowest one of 7.0 K km s^{-1} (3σ) and every 20 K km s^{-1} (white line) from the 6th one. (f) Integrated intensity distributions in $^{13}\text{CO}(J=1-0)$. The integration range is the same in the figure (e). Contours are plotted every 4 K km s^{-1} from 4 K km s^{-1} . (g) Velocity-galactic longitude diagram of loop 2. The velocity is smoothed at a resolution of 2.0 km s^{-1} . The integration range in the galactic latitude is from about 0.7° to 2.5° . Contours are plotted every 0.12 K deg from the lowest one of 0.20 K degree . (h) Velocity-galactic longitude diagram of loop 2. The velocity is smoothed at a resolution of 2.0 km s^{-1} . The integration range is the same as the figure (g). Contours are plotted every 0.05 K degree from 0.035 K degree .

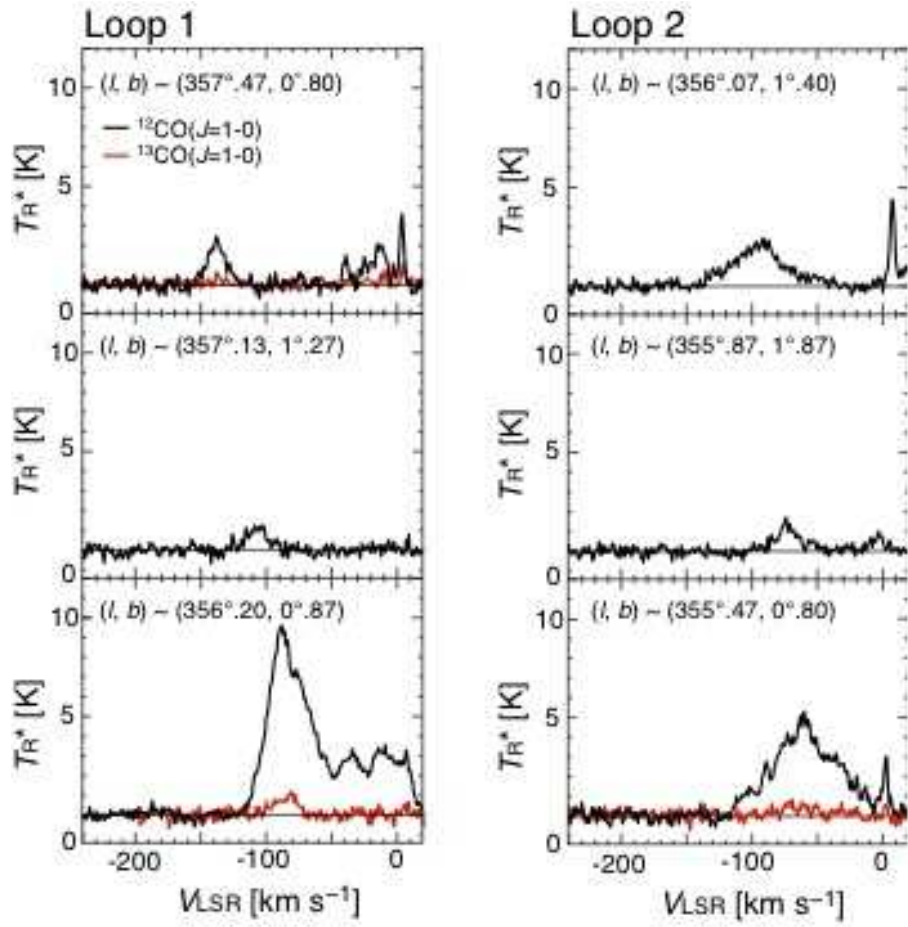


Fig. 4: Spectra of loops 1 and 2 in $^{12}\text{CO}(J=1-0)$ and $^{13}\text{CO}(J=1-0)$.

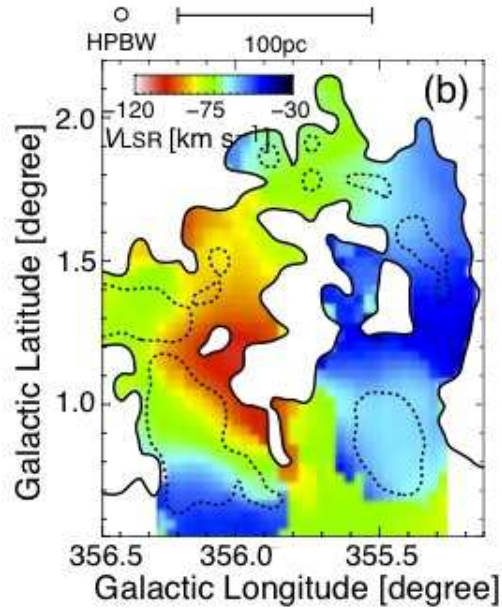
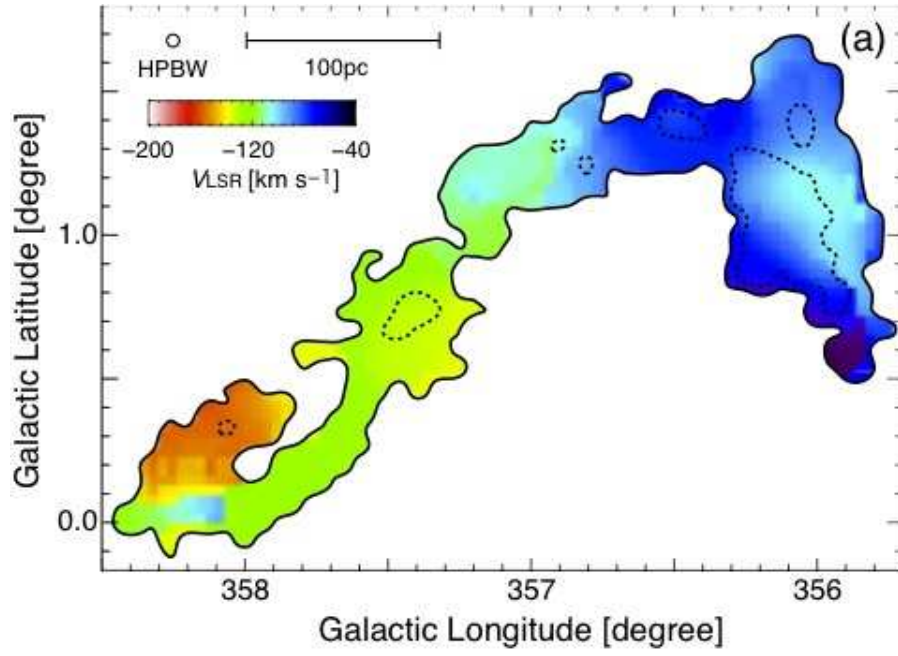


Fig. 5: Average velocity distributions of loops 1 and 2 in $^{12}\text{CO}(J=1-0)$. Contours in loops 1 and 2 are plotted at 5.2 K km s^{-1} (Bold contours) and 45.2 K km s^{-1} (dashed line).

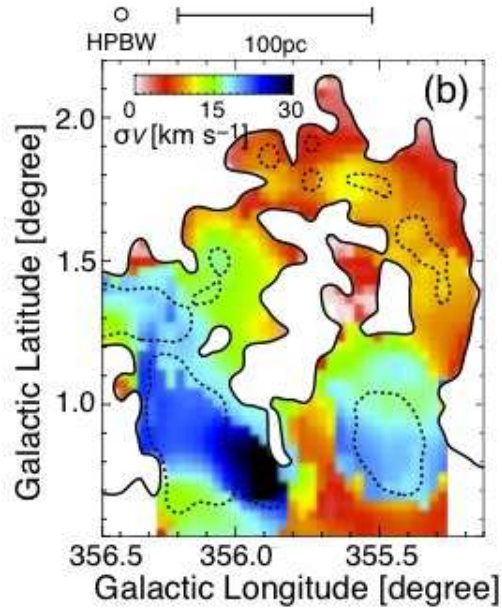
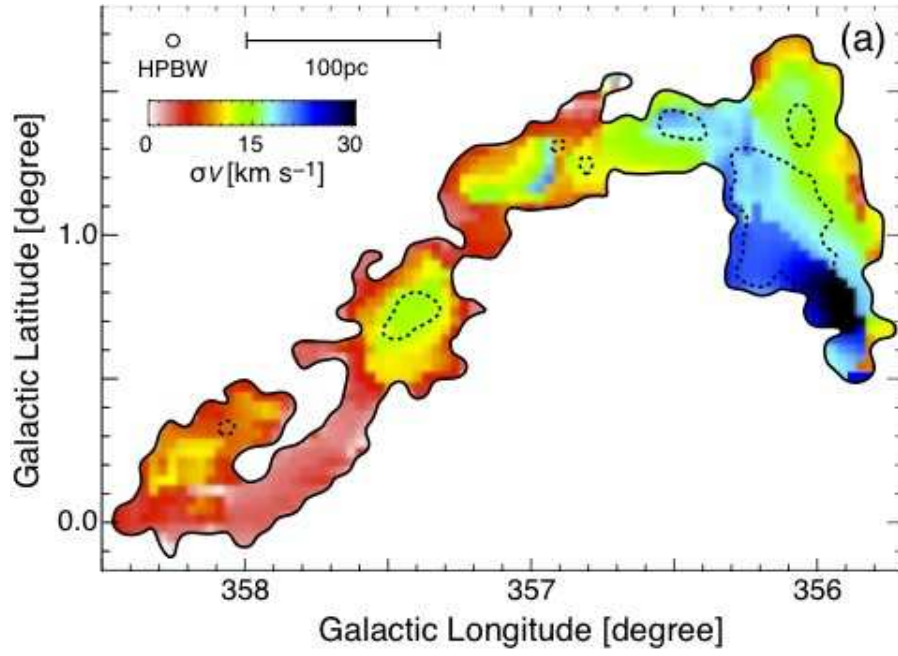


Fig. 6: Distributions of 1σ velocity dispersion of loops 1 and 2 in $^{12}\text{CO}(J=1-0)$. Contours in loops 1 and 2 are plotted at 5.2 K km s^{-1} (Bold contours) and 45.2 K km s^{-1} (dashed line).

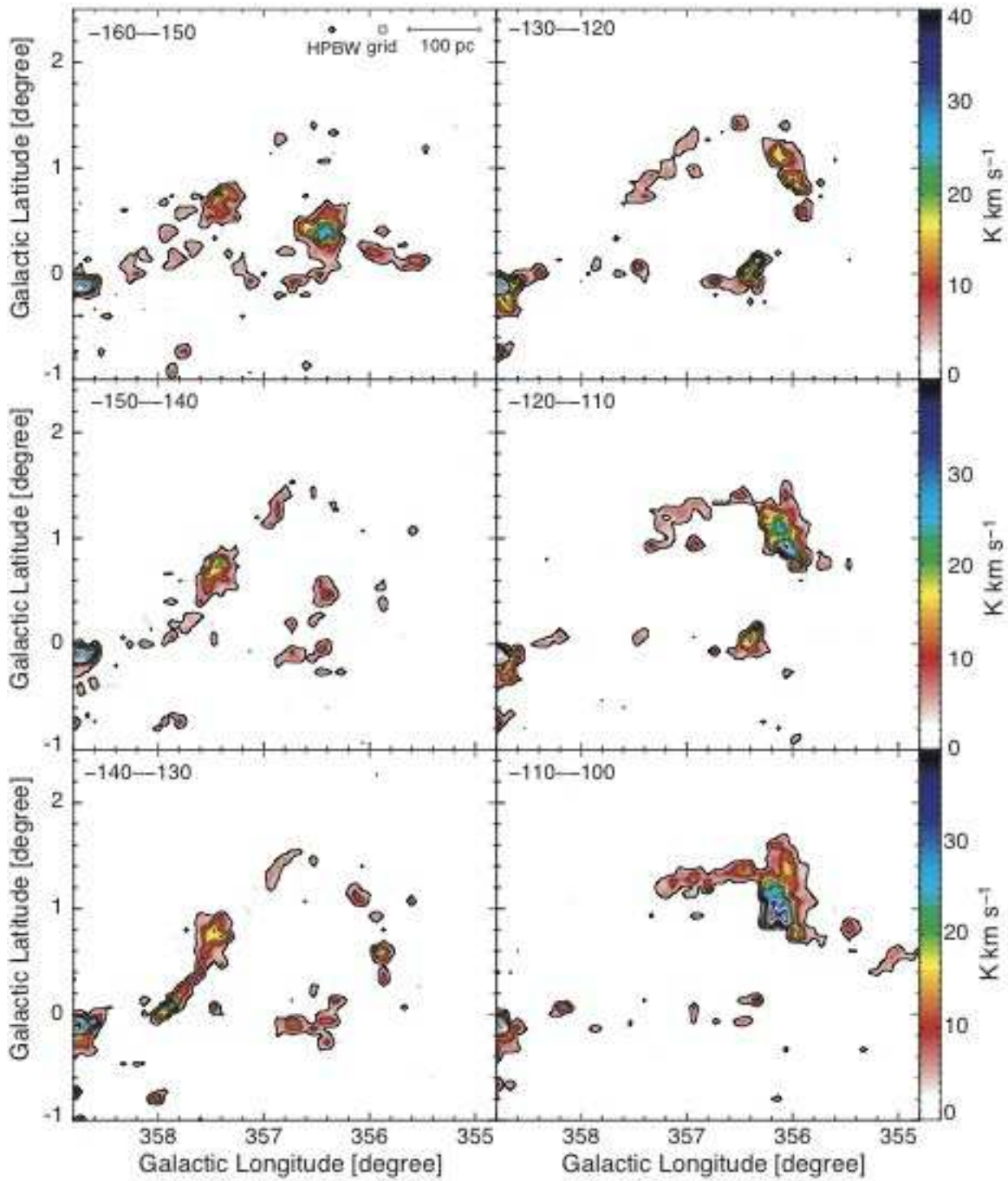


Fig. 7: Velocity channel maps of loops 1 and 2 in $^{12}\text{CO}(J=1-0)$ integrated over successive 10 km s^{-1} . Contours are plotted every 4.8 K km s^{-1} (black contours) from 3.6 K km s^{-1} and every 9.6 K km s^{-1} (white contours) from 32.4 K km s^{-1}

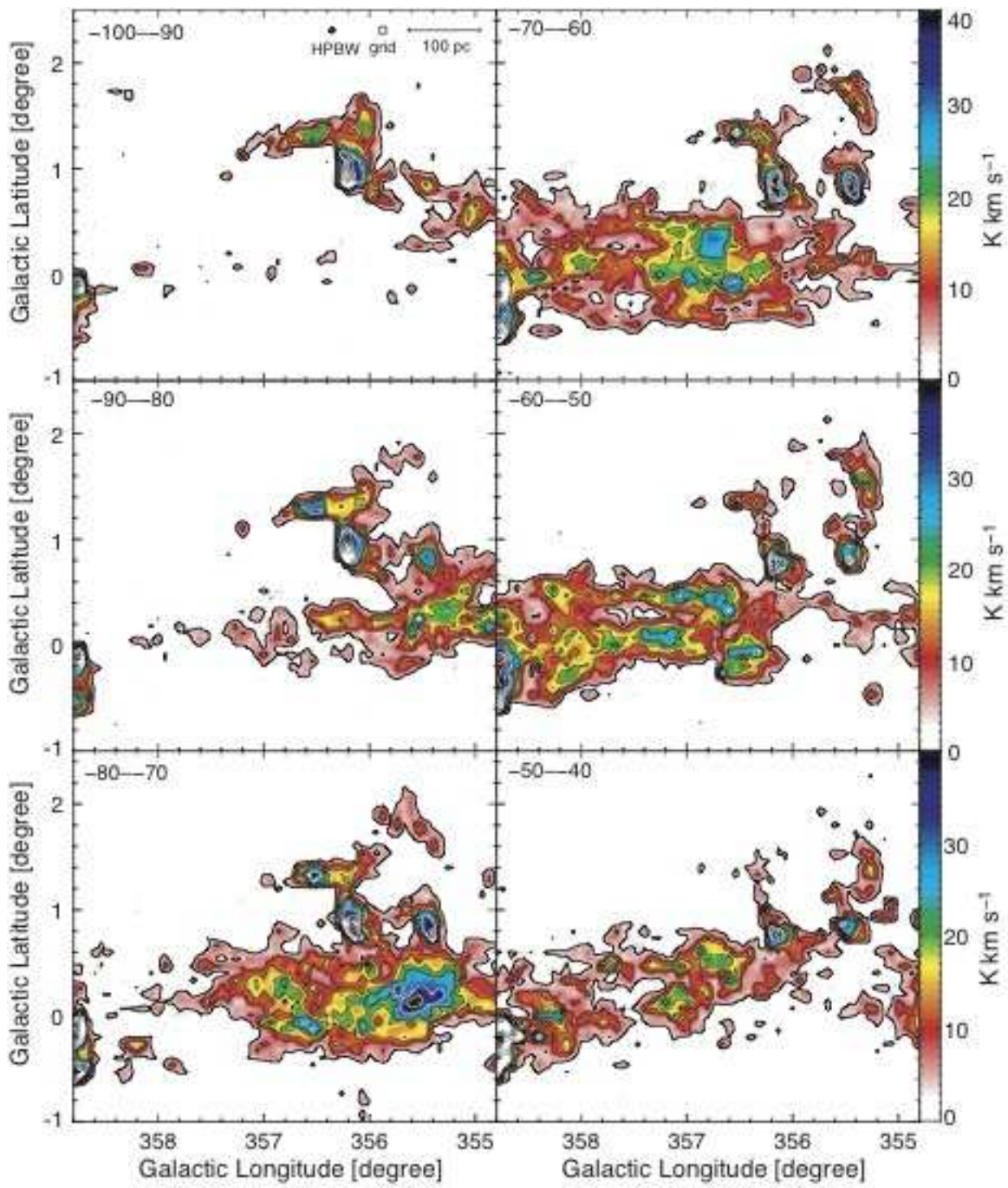


Fig. 7: continued.

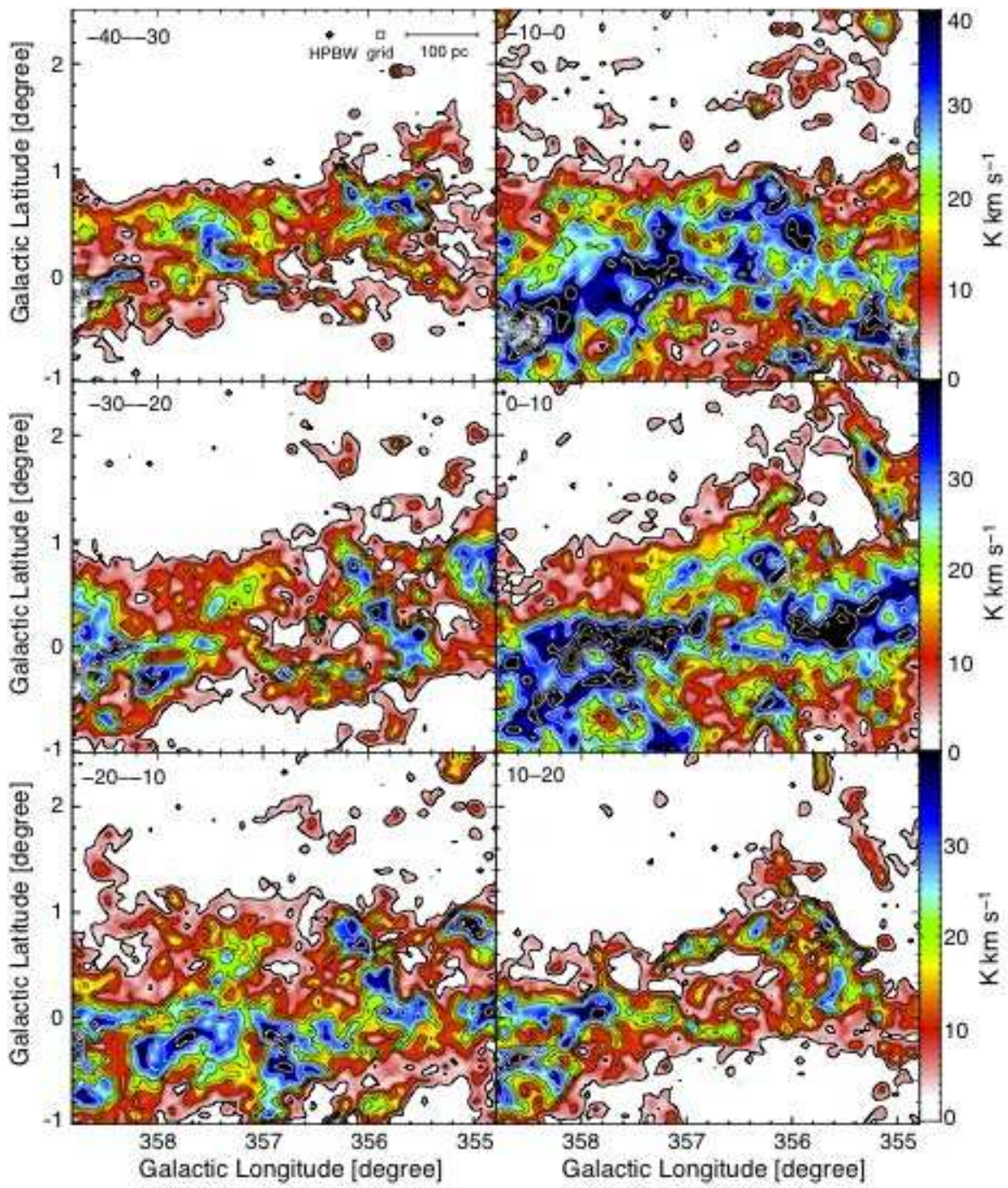


Fig. 7: continued.

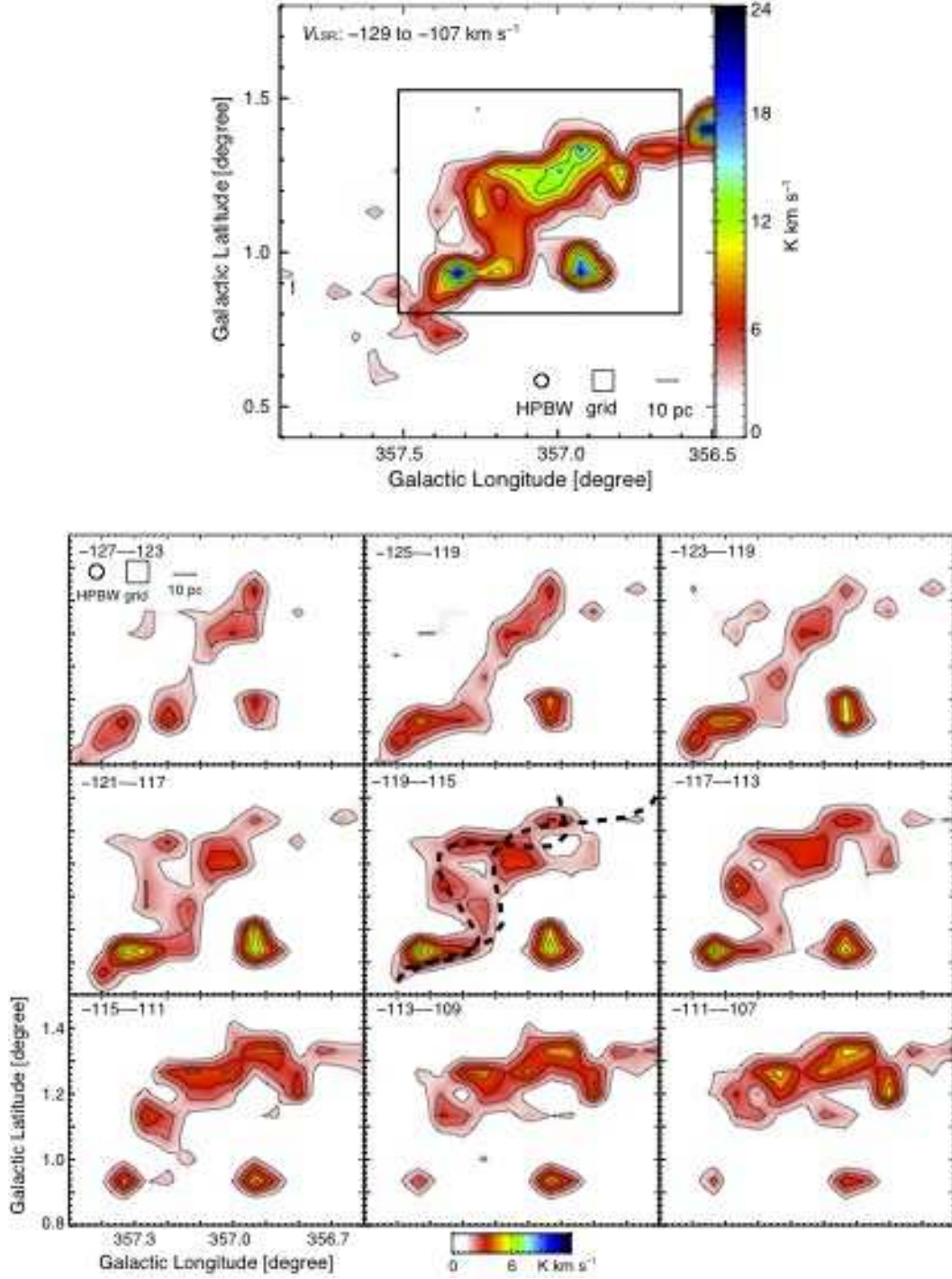


Fig. 8: Integrated intensity distributions of the helical distribution in loop 1. (a) Velocity integrated intensity map in $^{12}\text{CO}(J=1-0)$. The integration range is from -129 to -107 km s^{-1} . Contours are plotted every 2 K km s^{-1} from 2.6 K km s^{-1} . Black box indicates the region shown in figure (b). (b) Velocity channel maps of helical feature integrated over 4 km s^{-1} with interval of 2 km s^{-1} . Contours are plotted every 0.8 K km s^{-1} from 1.6 K km s^{-1} . Dotted lines show the fitting result with the parameters shown in Table 4.

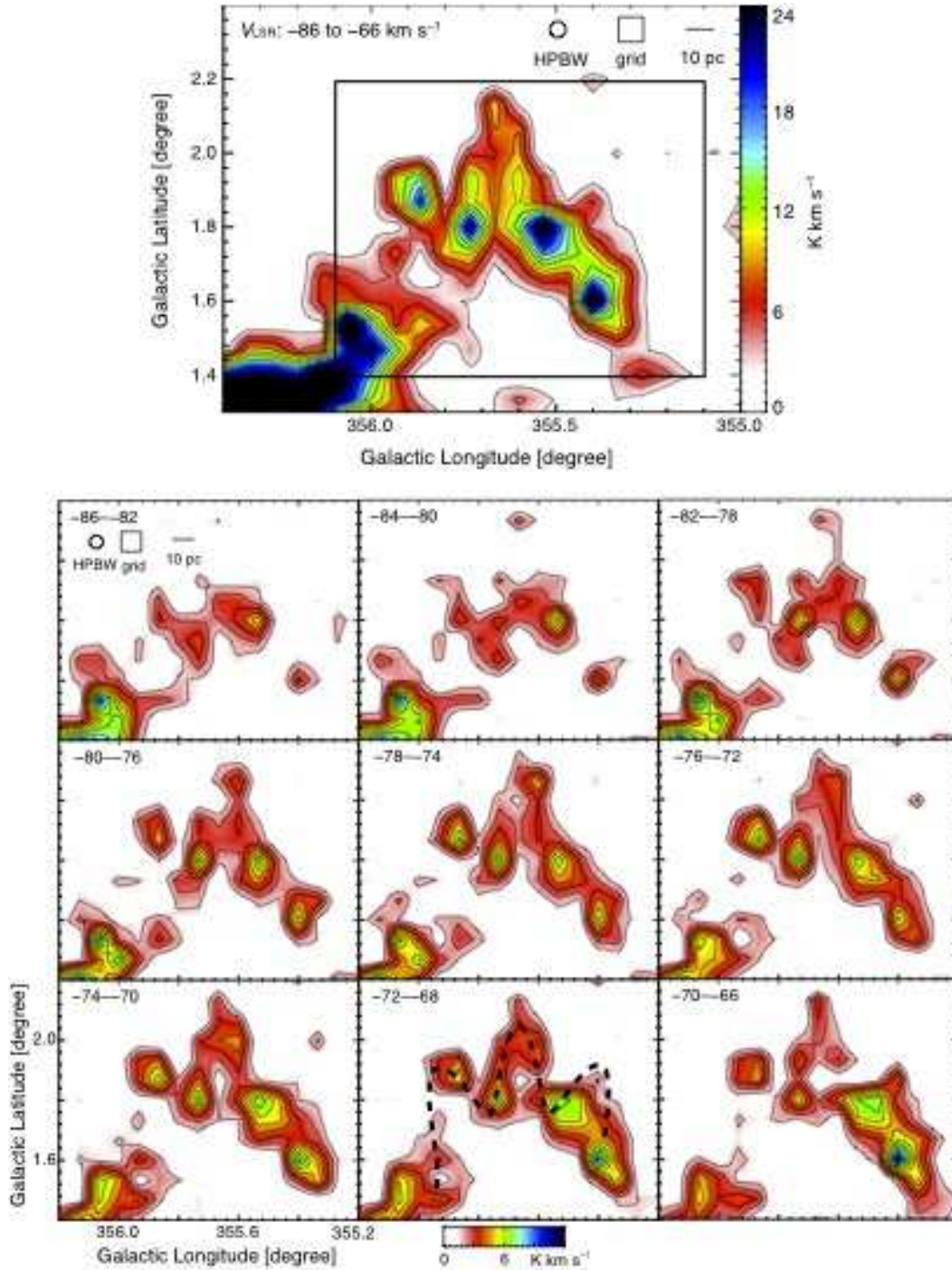


Fig. 9: Integrated intensity distributions of the helical distribution in loop 2. (a) Velocity integrated intensity map in $^{12}\text{CO}(J=1-0)$. The integration range is from -86 to -66 km s^{-1} . Contours are plotted every 2 K km s^{-1} from 2.6 K km s^{-1} . Black box indicates the region shown in figure (b). (b) Velocity channel maps of helical feature integrated over 4 km s^{-1} with interval of 2 km s^{-1} . Contours are plotted every 0.8 K km s^{-1} from 1.6 K km s^{-1} . Dotted lines show the fitting result with the parameters shown in Table 4.

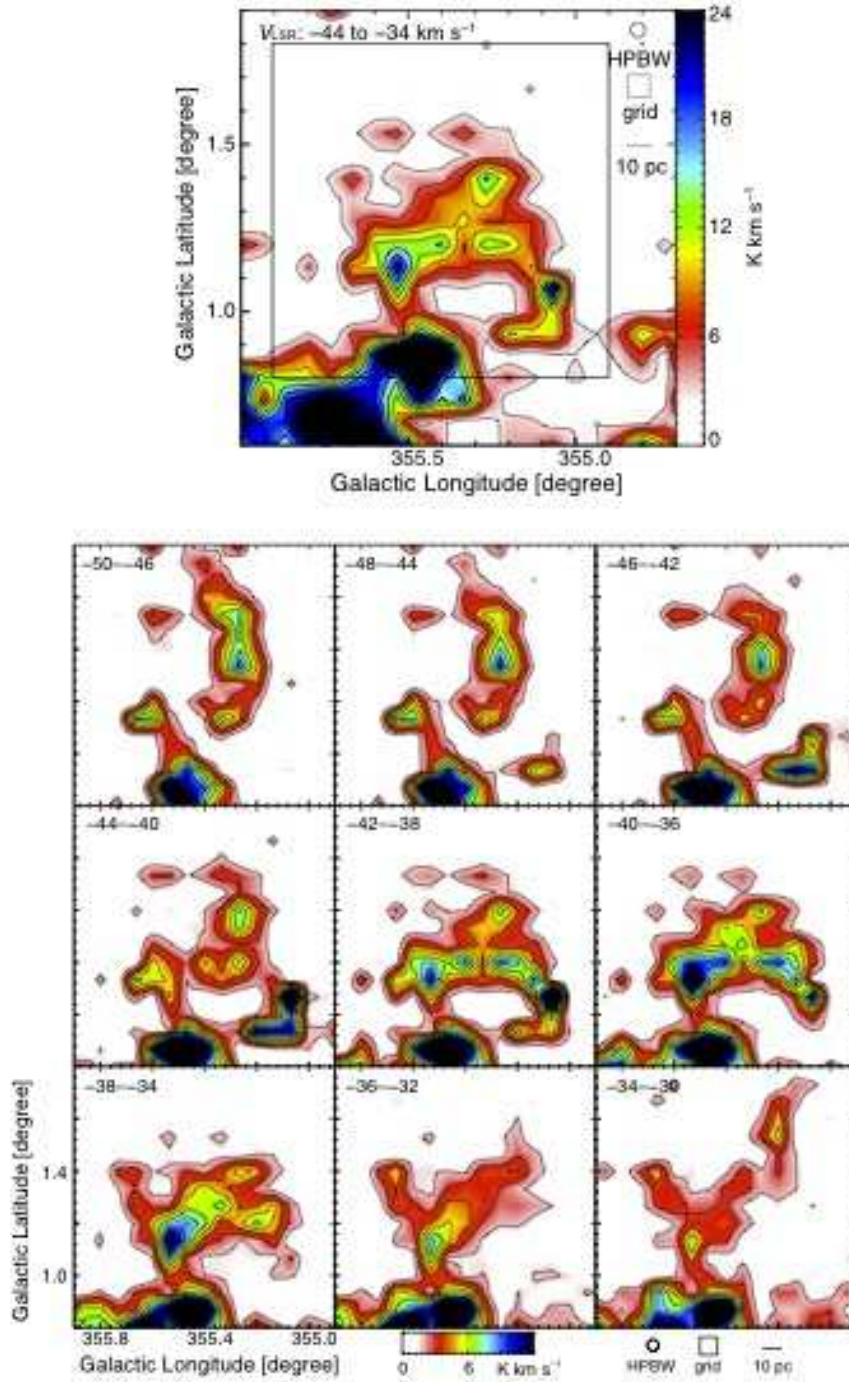


Fig. 10: Integrated intensity distributions of the helical distribution in loop 2. (a) Velocity integrated intensity map in $^{12}\text{CO}(J=1-0)$. The integration range is from -44 to -34 km s^{-1} . Contours are plotted every 2.4 K km s^{-1} from 2.6 K km s^{-1} . Black box indicates the region shown in figure (b). (b) Velocity channel maps of helical feature integrated over 4 km s^{-1} with interval of 2 km s^{-1} . Contours are plotted every 1.2 K km s^{-1} from 1.6 K km s^{-1} .

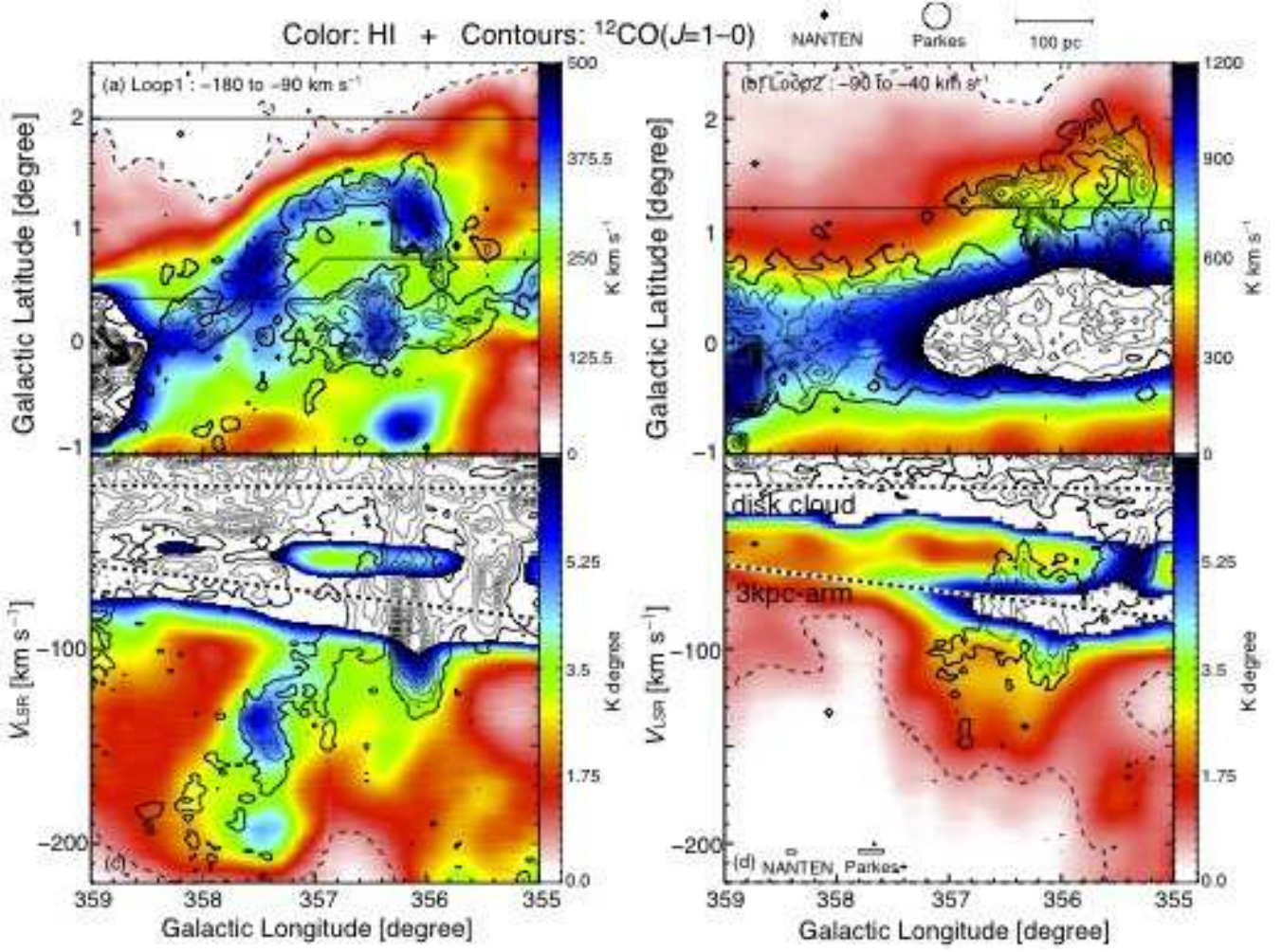


Fig. 11: Integrated intensity distributions of HI and $^{12}\text{CO}(J=1-0)$ emission. The color image and dashed contours indicate HI emission. Solid contours indicate $^{12}\text{CO}(J=1-0)$ emission. Dotted lines show 3-kpc arm and foreground disk components, respectively. (a) Velocity-integrated intensity maps of loop 1. Integration velocity range is from -180 to -90 km s^{-1} . HI: Contours are plotted at 42 K km s^{-1} . $^{12}\text{CO}(J=1-0)$: Contours are plotted every 4.8 K km s^{-1} from 3.6 K km s^{-1} and every 9.6 K km s^{-1} from 6th one. (b) Velocity-integrated intensity map of loop 2. Integration velocity range is from -90 to -40 km s^{-1} . Contours are plotted at the same levels in figure (a). (c) Galactic longitude-velocity diagram of loop 1. The integrated galactic latitude range is shown in figure (a) by solid lines. HI: Contours are plotted at 0.42 K degree . $^{12}\text{CO}(J=1-0)$: Contours are plotted every 0.2 K degree from 0.12 K degree . (d) Galactic longitude-velocity diagram of loop 2. Contours are plotted at the same levels of figure (c).

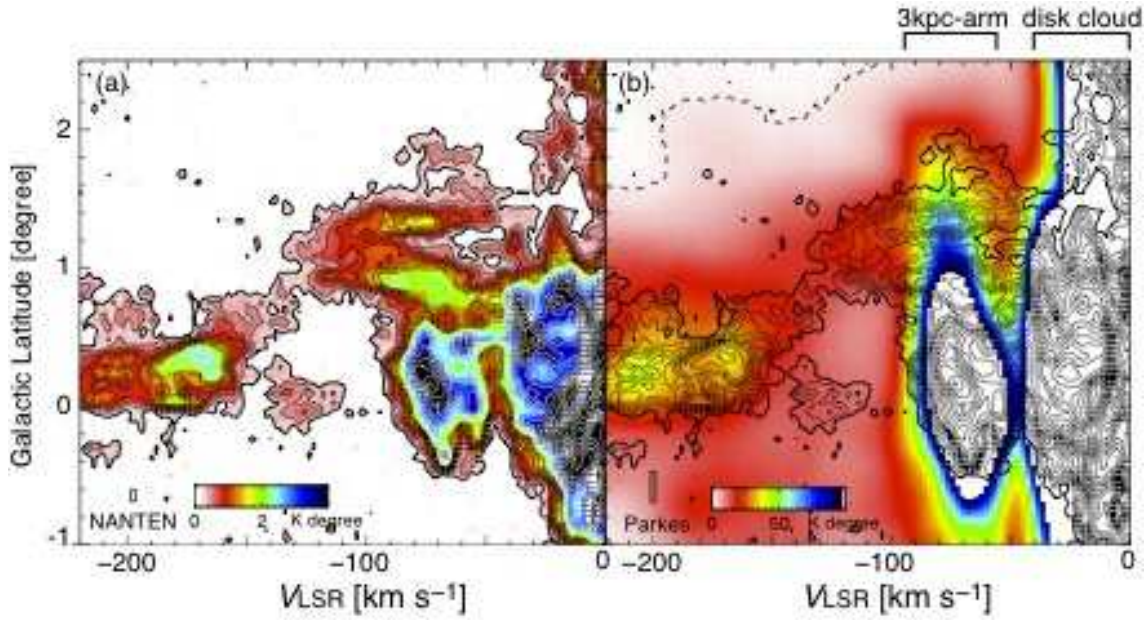


Fig. 12: (a) Velocity-galactic latitude diagram of loops 1 and 2 in $^{12}\text{CO}(J=1-0)$ integrated from 355° to 358° in galactic longitude. Contours are plotted every 0.2 K degree from 0.24 K (black) degree and every 0.4 K degree from 9th one (white). (b) Velocity-galactic latitude diagram of loops 1 and 2 of HI and CO integrated from 355° to 358° in galactic longitude. The color image and dotted contours indicate HI emission. Solid contours indicate $^{12}\text{CO}(J=1-0)$ emission. HI: Contours are plotted at 0.42 K degree. $^{12}\text{CO}(J=1-0)$: Contours are plotted at the same levels of figure (a).

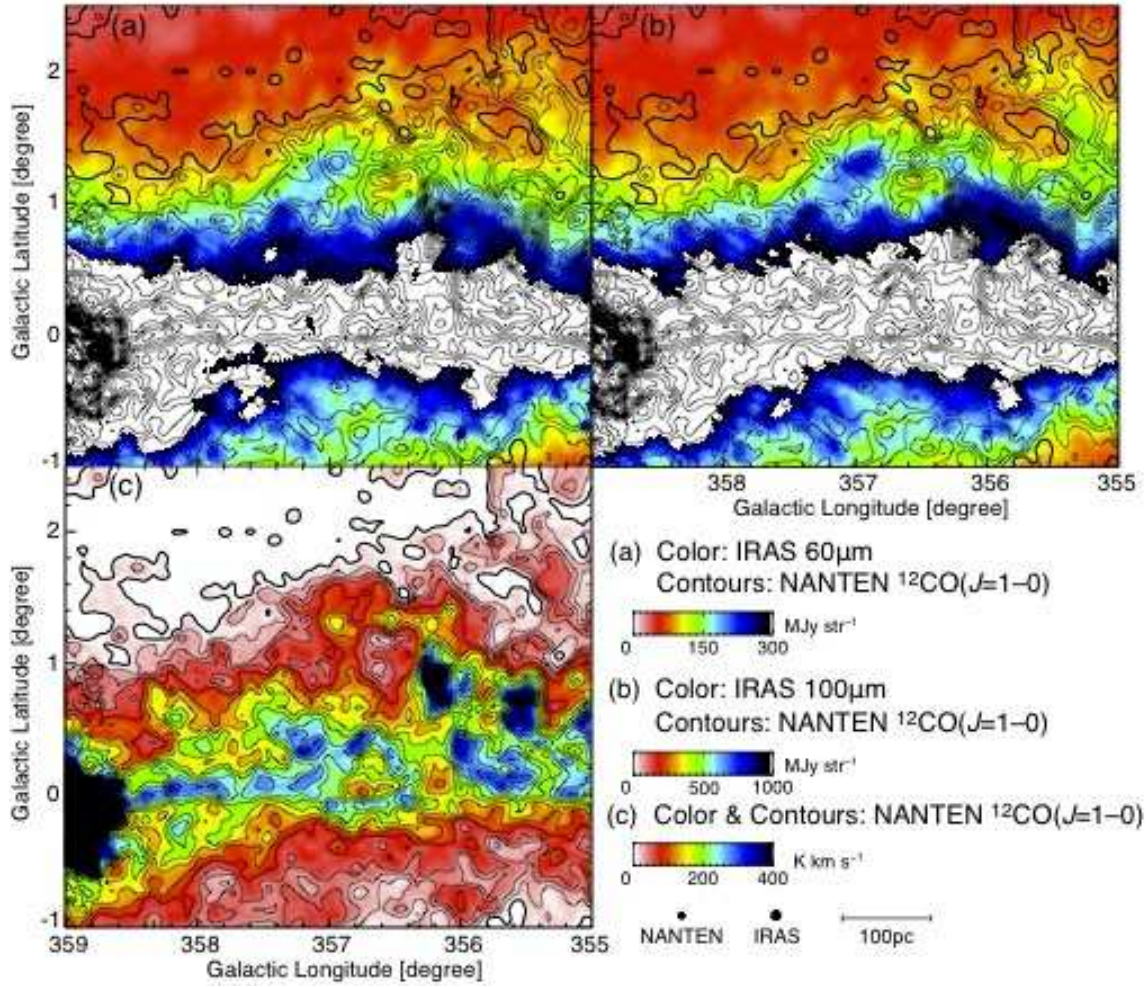


Fig. 13: (a, b) CO Integrated intensity distributions superposed on IRAS 60 μm (a) and 100 μm (b). Integration range of CO is from -300 to 300 km s^{-1} . Contours are plotted every 15 K km s^{-1} from 7 K km s^{-1} and every 30 K km s^{-1} from 5th one. (c) CO integrated intensity distributions without IRAS emission. Contour levels are the same with the figures (a) and (b).

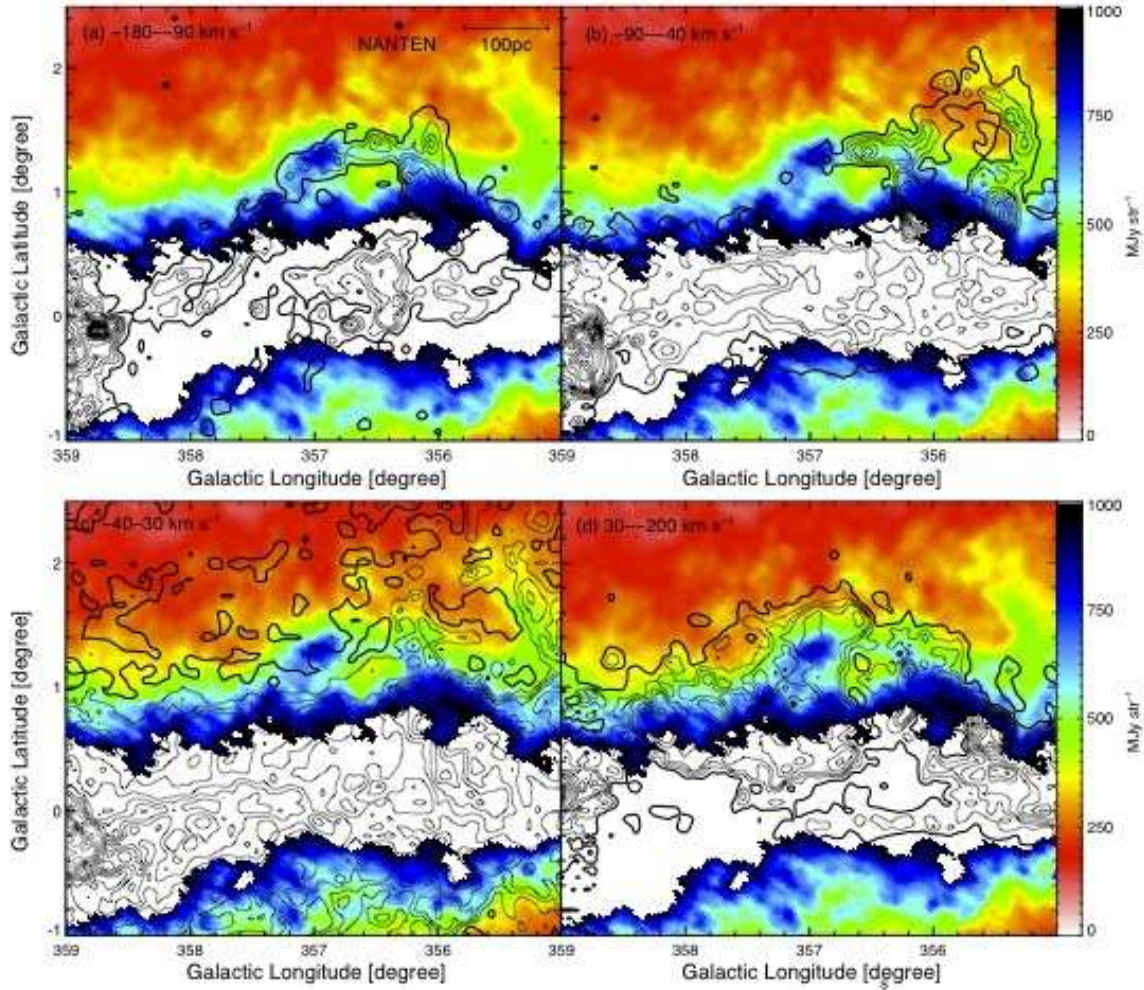


Fig. 14: CO Integrated intensity distributions superposed on $100 \mu\text{m}$. (a) Loop 1: Integration range is from -180 to -90 km s^{-1} . (b) Loop 2: Integration range is from -90 to -40 km s^{-1} . (c) Disk and local components: Integration range is from -40 to 30 km s^{-1} . (d) Loop 3: Integration range is from 30 to 200 km s^{-1} . Contours in all the figures are plotted every 15 K km s^{-1} from 7 K km s^{-1} and every 30 K km s^{-1} from 5th one.

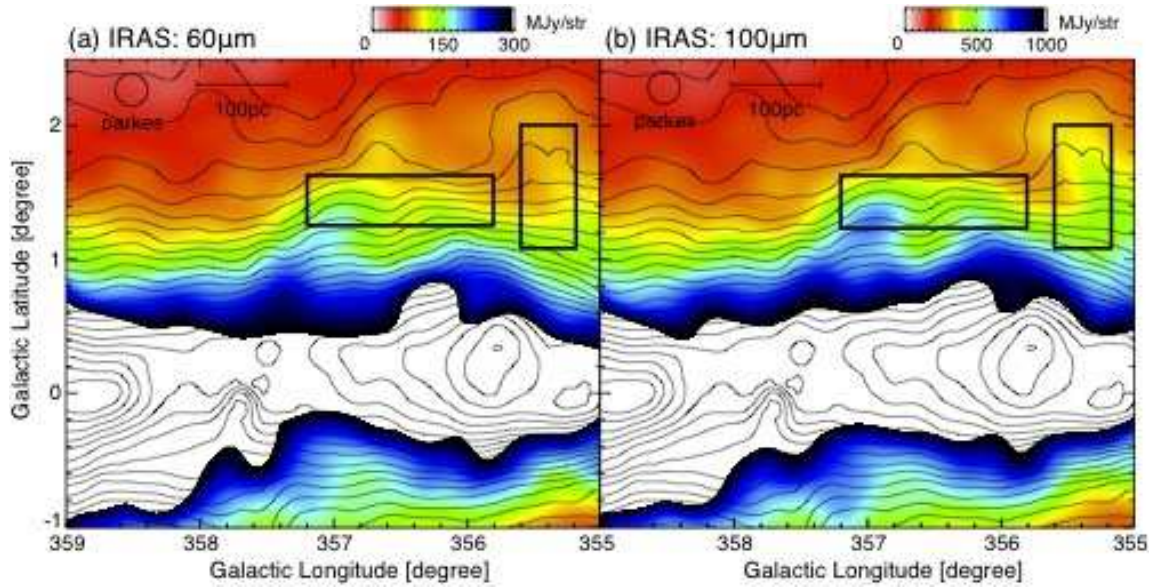


Fig. 15: HI integrated intensity distributions superposed on IRAS 60 μ m (a) and 100 μ m (b). Integration range of HI is from -300 to 300 km s^{-1} . Contours are plotted every every 300 K km s^{-1} from 100 K km s^{-1} . Black boxes show the regions for mass estimate in Figure 17

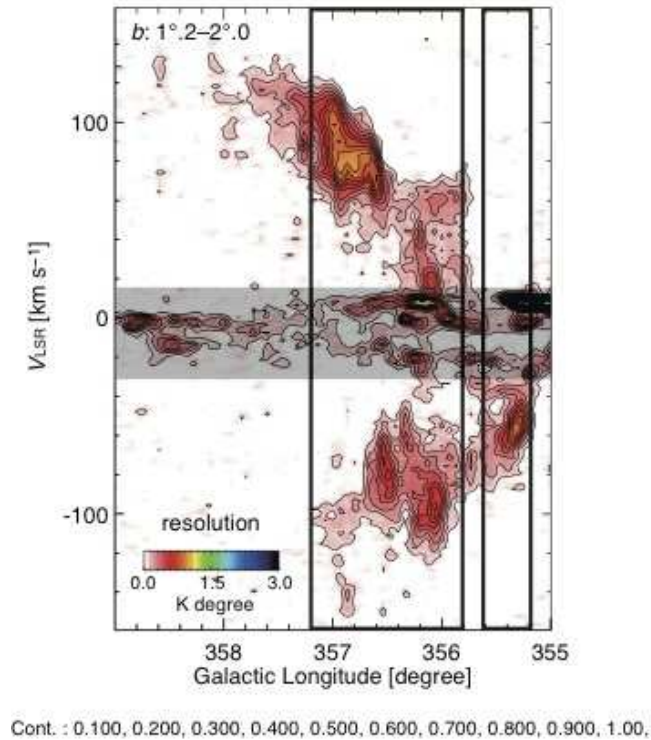


Fig. 16: Longitude-velocity diagram of the tops of the loops ($b \approx 1.2^\circ - 2.0^\circ$). Black boxes show the regions shown in Figure 15. Filled gray area shows the foreground emission, the extent of which in velocity is from -30 km s^{-1} to 15 km s^{-1} .

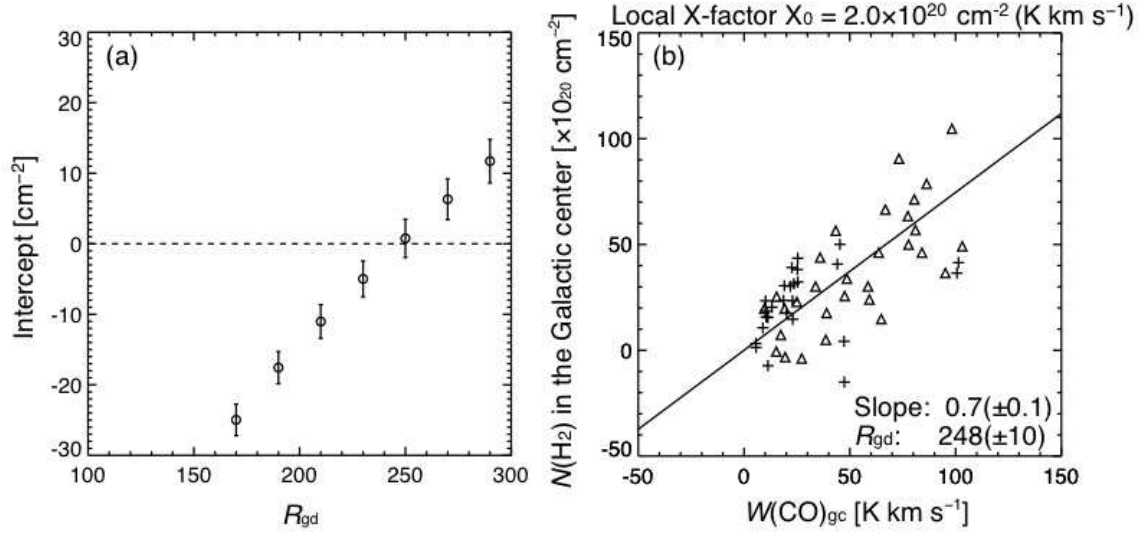


Fig. 17: (a) Variation of the intercept for different gas-dust ratio, R_{gd} . The intercepts were estimated by comparing between CO integrated intensity in the Galactic center, $W(\text{CO})_{\text{gc}}$, and H_2 column density in the Galactic center estimated with dust, HI and CO dataset by using equations (1)–(6). (b) Scatter plot of $W(\text{CO})_{\text{gc}}$ vs. $N(\text{H}_2)$ in the Galactic center for R_{gd} of 248. The triangles depict the top of loops 1 and 3, $(l, b) \simeq (355.8^\circ\text{--}357.2^\circ, 1.3^\circ\text{--}1.8^\circ)$ and the crosses depict the eastern part of the loop 2, $(l, b) \simeq (355.0^\circ\text{--}355.6^\circ, 1.1^\circ\text{--}2.0^\circ)$. Solid line shows the fitting result.

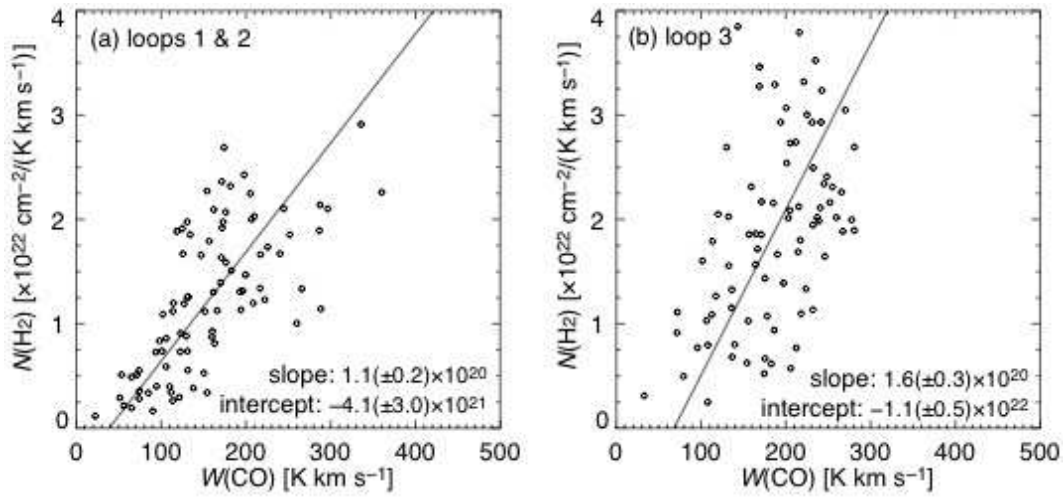


Fig. 18: Scatter plot of the CO integrated intensity of loops 1 and 2 and loop 3, $W(\text{CO})$, vs. the column density of molecular hydrogen estimated from ^{13}CO in the loops, $N(\text{H}_2)$. Solid line in each image shows the fitting result.

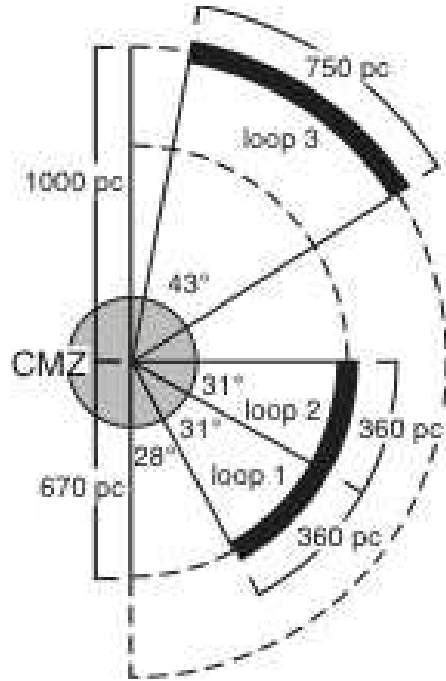


Fig. 19: A schematic image of the geometry of loops 1, 2 and 3 with face on view. The parameters in the figure are also summarized in Table 3.